

Comprehensive multiomic profiling of somatic mutations in malformations of cortical development

Changuk Chung^{1,2,#}, Xiaoxu Yang^{1,2,#}, Taejeong Bae³, Keng Ioi Vong^{1,2}, Swapnil Mittal^{1,2}, Catharina Donkels⁴, H. Westley Phillips⁵, Ashley P. L. Marsh^{1,2}, Martin W. Breuss^{1,2,6}, Laurel L. Ball^{1,2}, Camila Araújo Bernardino Garcia⁷, Renee D. George^{1,2}, Jing Gu^{1,2}, Mingchu Xu^{1,2}, Chelsea Barrows^{1,2}, Kiely N. James^{1,2}, Valentina Stanley^{1,2}, Anna Nidhiry^{1,2}, Sami Khoury^{1,2}, Gabrielle Howe^{1,2}, Emily Riley^{1,2}, Xin Xu^{1,2}, Brett Copeland^{1,2}, Yifan Wang³, Se Hoon Kim⁸, Hoon-Chul Kang⁸, Andreas Schulze-Bonhage⁹, Carola A. Haas^{4,9}, Horst Urbach¹⁰, Marco Prinz^{9,11}, Corrine Gardner¹², Christina A. Gurnett¹², Shifteh Sattar¹³, Mark Nespeca¹³, David D. Gonda¹³, Katsumi Imai¹⁴, Yukitoshi Takahashi¹⁴, Robert Chen¹⁵, Jin-Wu Tsai¹⁵, Valerio Conti¹⁶, Renzo Guerrini¹⁶, Orrin Devinsky¹⁷, Wilson A. Silva Jr¹⁸, Helio R. Machado⁷, Gary W. Mathern⁵, Alexej Abyzov³, Sara Baldassari¹⁹, St éphanie Boulac¹⁹, Focal Cortical Dysplasia Neurogenetics Consortium[&], Brain Somatic Mosaicism Network^{*} and Joseph G. Gleeson^{1,2,*}

¹Department of Neurosciences, University of California San Diego, La Jolla, CA, 92037, USA

²Rady Children's Institute for Genomic Medicine, San Diego, CA, 92123, USA

³Department of Quantitative Health Sciences, Center for Individualized Medicine, Mayo Clinic, Mayo Clinic, Rochester, MN, 55905, USA

⁴Department of Neurosurgery, Experimental Epilepsy Research, Medical Center-University of Freiburg, Faculty of Medicine, 79106 Freiburg, Germany

⁵Department of Neurosurgery, University of California at Los Angeles, CA, 90095, USA

⁶Department of Pediatrics, Section of Clinical Genetics and Metabolism, University of Colorado Aurora, CO, 80045, USA

⁷Laboratory of Pediatric Neurosurgery and Developmental Neuropathology, Dept. of Surgery and Anatomy, University of São Paulo (USP), Ribeirão Preto, 14000-000, Brazil

⁸Div Pediatric Neurology, Dept of Pediatrics, Severance Children's Hospital, Yonsei U College of Medicine, Seoul, Korea

⁹Center for Basics in NeuroModulation, Faculty of Medicine, University of Freiburg, 79106 Freiburg, Germany

¹⁰Department of Neuroradiology, Medical Center-University of Freiburg, Faculty of Medicine, 79106 Freiburg, Germany

¹¹Institute of Neuropathology, Medical Center-University of Freiburg, Faculty of Medicine, 79106 Freiburg, Germany

¹²St. Louis Children's Hospital, Washington University St Louis, MO, 63110, USA

¹³Epilepsy Center, Rady Children's Hospital, San Diego, CA, 92123, USA

¹⁴National Epilepsy Center, Shizuoka Institute of Epilepsy and Neurological Disorders, Shizuoka 420-8688, Japan

¹⁵Institute of Brain Science, National Yang-Ming University, Beitou 112, Taipei, Taiwan

¹⁶Paediatric Neurology Unit and Laboratories, A. Meyer Children's Hospital, University of Florence, Italy

¹⁷Epilepsy Service, Dept. Neurology, New York University, NY, 10016, USA

¹⁸Department of Genetics, Center for Cell-Based Therapy, Center for Integrative Systems Biology, University of São Paulo (USP), Ribeirão Preto, 14000-000, Brazil

¹⁹Paris Brain Institute - Institut du Cerveau - ICM, Hôpital Pitié-Salpêtrière - 47, bd de l'hôpital - 75013 Paris France

[#]These authors contributed equally

48 *Correspondence to: jogleeson@health.ucsd.edu
49 &Full membership of the FCD Neurogenetic Consortium is listed in the Supplement
50 ‡Full membership of the Brain Somatic Mosaicism Network is listed in the Supplement
51 Number of figures: 6, Number of extended data items: 7

52
53 Emails: chchung@health.ucsd.edu, xiy010@health.ucsd.edu, bae.taejeong@mayo.edu,
54 kivong@health.ucsd.edu, swmittal@ucsd.edu, catharina.donkels@uniklinik-freiburg.de,
55 carola.haas@uniklinik-freiburg.de, hphillips@mednet.ucla.edu, amarsh@health.ucsd.edu,
56 martin.breuss@cuanschutzz.edu, lball@health.ucsd.edu, camila.neurociencias@gmail.com,
57 reneegeorge@gmail.com, j3gu@ucsd.edu, mxu.china@gmail.com, cbarrows@ucsd.edu,
58 kiely.n.james@gmail.com, vstanley146@gmail.com, anidhiry@gmail.com,
59 samikhoury619@gmail.com, ghowe@ucsd.edu, eariley@ucsd.edu, virginiaxuxin@gmail.com,
60 brcopeland@gmail.com, paxco@yuhs.ac, hipo0207@yuhs.ac, [bonhage@uniklinik-freiburg.de](mailto:andreas.schulze-
61 bonhage@uniklinik-freiburg.de), carola.haas@uniklinik-freiburg.de, gardnerc@wustl.edu,
62 gurnette@wustl.edu, ssattar@ucsd.edu, mnespeca@ucsd.edu, dgonda@rchsd.org, [ped@umin.ac.jp](mailto:takahashi-
63 ped@umin.ac.jp), roberthhchen3@gmail.com, jinwu.tsai@gmail.com, valerio.conti@meyer.it,
64 renzo.guerrini@meyer.it, wilsonjr@usp.br, od4@nyu.edu, hrmachad@fmrp.usp.br,
65 gmathern@ucla.edu, jogleeson@health.ucsd.edu

66
67 **Abstract: 129 words, Manuscript: 3101 words, Figures: 6, Extended Data items: 7, Suppl**
68 **Tables: 3**

69 **Keywords: epilepsy, focal cortical dysplasia, brain mosaicism, mTOR, single-cell**
70 **sequencing, whole exome sequencing**

71 72 **Abstract**

73 Malformations of cortical development (MCD) are neurological conditions displaying focal
74 disruption of cortical architecture and cellular organization arising during embryogenesis, largely
75 from somatic mosaic mutations. Identifying the genetic causes of MCD has been a challenge, as
76 mutations remain at low allelic fractions in brain tissue resected to treat epilepsy. Here, we report
77 a genetic atlas from 317 brain resections, identifying 69 mutated genes through intensive
78 profiling of somatic mutations, combining whole-exome and targeted-amplicon sequencing with
79 functional validation and single-cell sequencing. Genotype-phenotype correlation analysis
80 elucidated specific MCD gene sets associating distinct pathophysiological and clinical
81 phenotypes. The unique spatiotemporal expression patterns identified by comparing single-
82 nucleus transcriptional sequences of mutated genes in control and patient brains implicates
83 critical roles in excitatory neurogenic pools during brain development, and in promoting
84 neuronal hyperexcitability after birth.

85 86 **Introduction**

87 MCDs are heterogeneous groups of neurodevelopmental disorders with localized malformation
88 of cortical structures, often presenting with intractable epilepsy¹. Major MCD subtypes include
89 different classes of focal cortical dysplasia (FCD), hemimegalencephaly (HME), and tuberous
90 sclerosis complex (TSC)². The International League Against Epilepsy (ILAE) has classified FCD
91 subtypes based upon neuropathological features and cell types³. MCD patients are often undergo

92 surgical resection of the lesion to treat drug-refractory epilepsy, which has led to remarkable
93 clinical benefit in published series⁴. The abnormal histology of resected regions includes loss of
94 lamination of cortical layers, enlarged dysplastic neurons or balloon cells, sometimes
95 accompanied by other brain abnormalities. But similar to brain tumors, it can be difficult to
96 predict pathology prior to surgery.

97 Again, like with brain tumors, genetic studies may offer insights into mechanisms.
98 Somatic mTOR pathway gene mutations are frequently detected in HME and type II FCD foci^{5,6}.
99 Recently, small- or medium-size cohort studies (<100 cases) have confirmed these results and
100 have correlated defects in neuronal migration, cell size and neurophysiology⁷. Still, the vast
101 majority of MCD cases still remain genetically unsolved, suggesting other genes or modules
102 contribute to MCD.

103 Detecting mutant alleles in bulk resected foci from MCD patients is challenging because
104 unlike in brain tumors, the mutant cells in MCD are probably not hyperproliferative, and thus
105 variant allelic fraction (VAF) are often <5%, diluted by genomes of surrounding non-mutated
106 cells⁸. Fortunately, new computational algorithms have helped reduce false-positive and false-
107 negative signals, even when no ‘normal’ paired sample is available for comparison⁹⁻¹¹. The NIH-
108 supported Brain Somatic Mosaicism Network established the ‘BSMN common pipeline’,
109 incorporating a ‘best practice’ workflow to reliably and reproducibly identify somatic variants
110 contributed by members of the Network¹². With these advances, we thus assessed the possibility
111 of gene networks beyond mTOR that could underlie MCDs. This new gene discovery may give
112 insights on novel druggable pathways in cases of incomplete resection due to regional
113 importance or drug-resistant forms of MCD.

114

115 **Results**

116 **The genetic landscape of MCD from targeted and unbiased sequencing**

117 To perform a thorough genetic screening of somatic mutations in resected epileptic tissue, we
118 formed the FCD Neurogenetics Consortium and enrolled 327 samples that met clinical and
119 pathological criteria for FCD or HME. We excluded TSC from our enrollment criteria because
120 genes are already well known. Our cohort included 31 HME cases, 98 type I-, 142 type II-, 32
121 type III-, and 12 unclassified-FCD cases. We included acute resected brain from 10
122 neurotypicals and 2 TSC cases for comparison (Fig. 1a, supplementary table 1). Patients with
123 environmental causes, syndromic presentations, inherited mutations, multifocal lesions, or
124 tumors were excluded (Methods).

125 We used a three-phase genetic screening, each followed by filtering for likely causative
126 mutations using published methods^{13,14}, and each followed by orthogonal targeted amplicon
127 sequencing (TASeq) intra-case validation and VAF quantification compared with controls
128 (~5000 X, TASeq)(Fig. 1b). In Phase 1, we performed amplicon sequencing (AmpliSeq, ~1000
129 X) profiling the entire open reading frame of 87 genes previously detected in FCD/HMEs or
130 known PI3K-AKT3-mTOR interactors (‘MCD panel v1’, Supplementary Table 2a). In Phase 2,
131 for 75 unsolved cases from Phase 1 and additionally collected 54 cases, we performed unbiased
132 deep whole-exome sequencing (WES, ~300 X) on paired samples, where available, or on
133 unpaired samples (i.e. brain plus blood/saliva vs. brain only). In Phase 3, from an additional
134 subcohort of 132 new cases, we designed the ‘MCD panel v2’ (Supplementary Table 2b)
135 including known and novel genes detected in Phases 1 and 2 (Extended Data Fig. 1, Methods).
136 We re-sequenced unsolved cases from Phase 2, expecting that the higher read depth afforded by

137 panel sequencing could provided greater sensitivity to detect low VAF mutations, and used
138 BSMN best practice guidelines for mapping and variant calling¹².

139 From Phases 1 to 3, 1181 candidate somatic SNVs were identified. Of these, 628 were
140 excluded based on gnomAD allele frequencies, dinucleotide repeats, homopolymers, and
141 additional BSMN established criteria (Methods)^{15,16}. This yielded 554 candidate somatic SNV
142 that were further assessed by TASEq, yielding 108 validated somatic SNV calls (19.4%
143 validation rate, Fig. 1c, Supplementary Table 3), similar to other BSMN effort validation rates
144 ^{12,17}. In detail, 15, 67 and 26 validated somatic SNV calls were derived from phase 1, 2 and
145 phase 3, respectively. The measured VAFs between the AmpliSeq/WES and TASEq were
146 correlated as expected ($R^2=0.7243$) (Fig. 1d). Of the 69 candidate MCD genes mutated in 76
147 patients, 8 were recurrently mutated, including known mTOR pathway genes as well as several
148 novel candidates (Fig. 1e).

149 We estimate only ~7% of mutations identified are likely attributable to false discovery
150 during variant calling, based upon background mutation rate in 75 BSMN neurotypical brain
151 samples, and published experience from the BSMN^{12,18}, processed with the same workflow (see
152 Methods). Thus, 93% of our candidate MCD mutations would not have been identified in a size-
153 matched neurotypical control cohort.

154 Most patients (80.52%, 62 cases) showed a single somatic mutation, but some showed two
155 somatic mutations (14.29%, 11 cases), and some showed more than two mutations (5.19%, 4
156 cases). Interestingly, HME-4144 showed 11 different somatic mutations, all of which were
157 validated with TASEq. Although there are several possible explanations for HME-4144, we
158 expect this reflects clonal expansion from a driver mutation, with detection of multiple passenger
159 mutations, as reported in brain tumors¹⁹.

160 Single-base mutational signatures (SBS) were developed to describe potential mutational
161 mechanisms in human disease²⁰. We found 60.2% of mutations were C>T, likely arising from
162 DNA epigenetic marks²¹ (Extended Data Fig. 2). Enrichment of SBS1 and SBS5, clock-like
163 mutational signatures suggest endogenous mutations arising during corticogenesis DNA
164 replication.

165

166 **Functional dissection of the MCD genes**

167 Interestingly, most validated genes were non-recurrently mutated (88.4%, 61 of 69) in our
168 cohort, suggesting substantial genetic heterogeneity in MCD. This nevertheless provided an
169 opportunity to study converging functional gene networks. Thus, we performed Markov
170 clustering with a STRING network generated from the putative MCD genes²², as well as recently
171 reported novel MCD candidates (*NAV2*, *EEF2*, *CASK*, *NF1*, *KRAS*, *PTPN11*)^{23,24} (Fig. 2a). We
172 identified four clusters, with cluster 1 (“mTOR pathway”) showing the highest term enrichment
173 to the mTOR/MAP kinase signaling, supporting prior results for Type II MCDs. Cluster 1 also
174 highlighted newly identified genes *FGFR2*, *KLHL22*, *RRAGA*, *PPP2R5D*, *PIK3R3*, *EEF2*,
175 *EIF4G1*, and *MAPK9*. Cluster 2 identified “Calcium Dynamics” and included genes *ATP2A1*,
176 *RYR2*, *RYR3*, *PSEN2*, *TTN*, *UTRN*. Cluster 3 labeled “Synaptic Functions” and included genes
177 *CASK*, *GRIN2C*, and *PPFIA4*. Cluster 4 labeled “Gene Expression” and included intellectual
178 disability genes, mostly involved in nuclear function, including *NUP214*, *PRR14*, *PCNT*, *NIPBL*,
179 *SRCAP*, *ASH1L*, *TRIP12*, and *MED13* (Fig. 2b).

180 Notably, *ATP2A1*, *PPFIA4*, and *NIPBL* were recurrently mutated, either within our
181 cohort or with a recent report²⁴ (Extended Data Fig. 3a-b), occurring withing the latter 3 clusters.

182 While these clusters were not previously reported in MCDs, they were previously implicated in
183 epilepsy, neurodevelopmental and neurodegenerative disease^{25,26}, suggesting functional overlap
184 with MCDs. We further performed ClueGO analysis and found enrichment in mTOR signaling,
185 focal adhesion assembly, cardiac muscle cell contraction, and artery morphogenesis (Extended
186 Data Fig. 4). ClueGO also displayed isolated gene ontology (GO) term clusters such as ‘calcium
187 ion import’ and ‘protein localization to synapse’.

188

189 **Functional validation of selected module genes in embryonic mouse brain**

190 To investigate the roles of novel MCD genes and modules, we selected two potential mTOR
191 pathway mutations (*RRAGA* p.H226R, *KLHL22* p.R38Q), and non-mTOR gene mutation
192 (*GRIN2C* p.T529M), discovered in FCD-7967, 3560, and 5157, respectively. *RRAGA* encodes
193 Ras-related GTP binding A (RAGA), a GTPase sensing amino acid and activating mTOR
194 signaling, with two functional domains: GTPase domain and C-terminal ‘roadblock’ domain
195 (CRD)²⁷. The mosaic p.H226R mutation occurs within the CRD, which binds to the RAGB
196 protein and is conserved throughout vertebrate evolution (Extended Data Fig. 3c) and thus could
197 change binding affinity. *KLHL22* encodes a CUL3 adaptor, determining E3 ubiquitin ligase
198 specificity. The CUL3-*KLHL22* complex mediates degradation of DEPDC5, required for
199 MTORC1 activation²⁸. The *KLHL22* p.R38Q variant in FCD-3560 is near the BTB (Broad-
200 Complex, Tramtrack and Bric a brac) domain that interacts with CUL3 (Extended Data Fig. 3d),
201 suggesting the variant could enhance MTORC1 activity. *GRIN2C* encodes a subunit of the
202 NMDA receptor regulating synaptic plasticity, memory, and cognition^{29,30}, dysfunction of which
203 is implicated in many neurocognitive diseases including epilepsy, neurodevelopment, and
204 tumors^{31,32}. *GRIN2C* p.T529M mutation is located in the S1 glutamate ligand-binding domain
205 (S1 LBD) (Extended Data Fig. 3e). *GRIN2A* p.T531M mutation, an analog mutation of *GRIN2C*
206 p.T529M in our cohort, was previously reported in epilepsy-aphasia spectrum disorders, where it
207 increased NMDA receptors ‘open-state’ probability³². This suggests that the p.T529M mutation
208 activates the channel, likely in an mTOR independent fashion. Thus, all mutations assessed here
209 are likely gain-of-function and exert functional impact on cells in which they are expressed.

210 To test this hypothesis, we introduced mutant or wildtype (WT) genes co-expressing
211 enhanced green fluorescent protein (EGFP) into the dorsal subventricular zone via
212 electroporation at mouse embryonic day 14 (E14), then harvested tissue at either E18 to assess
213 migration, or at postnatal day 21 (P21) to assess cell size and phospho-S6 as a reporter of mTOR
214 activity³³ (Fig. 3a). In E18 cortices, we found EGFP-positive cells expressing mutant but not WT
215 forms of *RRAGA* and *KLHL22* showed significant migration defects of varying severity, whereas
216 mutant *GRIN2C* showed no defect (Fig. 3b). These migration defects in *RRAGA* and *KLHL22*
217 mutant cells replicate major findings of MCD disrupted cortical architecture.

218 We next assessed cellular phenotype at P21 with samples available in both mice and the
219 corresponding patients, and found enlarged cell body area in both mutant form of *KLHL22* and
220 *GRIN2C* compared to according wildtype. In contrast, the elevated levels of pS6 staining,
221 described previously in association with mTOR pathway mutations⁶, was found only in mutant
222 *KLHL22*, but not in mutant *GRIN2C* mice (Fig. 3c).

223 To assess correlation with human samples, we assessed archived neuropathological tissue
224 sections for histology and pS6 activity. Similar to our mouse models, we found patient FCD-
225 3560 carrying *KLHL22* p.R38Q showed enlarged neurons that co-stained for excess pS6 staining,
226 whereas FCD-5157 carrying *GRIN2C* p.T529M showed only a slight increase in cell body size

227 and no evidence of excessive pS6 staining (Fig. 3d). While this analysis does not take into
228 account the genotype of individual cells, it suggests *KLHL22* but not *GRIN2C* mutations impact
229 mTOR signaling.

230

231 **Genotype-phenotype correlations in MCD patients**

232 To assess the phenotypic contributions of the MCD genes we found, we focused on 76 of our
233 ‘genetically solved’ MCD cases, comparing detailed neuropathology, brain imaging, and clinical
234 course. We performed Pearson correlation followed by hierarchical clustering based upon ILAE
235 neuropathological diagnosis, compared with GO term-based curated genesets and whether the
236 genetic variant was present in COSMIC DB (Methods, Supplementary Table 3,4, Fig. 4). We
237 found that FCD Type IIA and Type IIB, and HME were more tightly clustered than FCD Type I
238 or III (Fig. 4a), likely reflecting shared neuropathological features that include large dysplastic
239 neurons. As expected, FCT Type IIA, Type IIB, and HME were positively associated with the
240 mTOR pathway GO term and COSMIC DB entry, FCD Type III, however, was associated with
241 the MAPK pathway, consistent with recent publications implicating *BRAF*, *FGFR2*, *NOD2*, and
242 *MAPK9* in their etiology³⁴⁻³⁶. FCD Type I showed few strong positive correlations except for
243 Glycosylation, consistent with recent associations with *SLC35A2* and *CANTI*^{37,38}.

244 We next investigated correlations between clinical phenotypes extracted from detailed
245 medical records including seizure type, neuropsychological examination, and positron emission
246 tomography (PET) metabolism, often used to help localize seizure focus^{39,40}. Seizure frequency,
247 early age of onset, Engel score, and history of infantile spasms drove clinical clustering, likely
248 reflecting shared clinical features in the most challenging patients. Focusing on the correlations,
249 PET hypometabolism correlated positively with COSMIC DB entry, and negatively with MAPK
250 and Ubiquitination (Fig. 4b), suggesting divergent metabolic mechanisms. Abnormal
251 neurological examination correlated positively with COSMIC DB entry and negatively with
252 Type I histology, which may reflect the effects of mutations on baseline neurological function.

253

254 **MCD genes enriched in the excitatory neuronal lineage**

255 To infer the cell type in which MCD genes function, we accessed a published single-cell
256 transcriptome dataset from the 2nd-trimester human telencephalon, at a time when these
257 mutations probably arose⁴¹ (Fig. 5a). We generated an eigengene, by mapping the average
258 expression of our MCD genes against the UMAP plot (Fig. 5b). This showed a strong positive
259 correlation with dividing radial glial cells, a moderate correlation in dividing intermediate
260 progenitor cells (IPCs) and mature excitatory neuron cells. We found a negative correlation with
261 inhibitory neuronal lineages including medial and central ganglionic eminences (MGE, CGE)
262 and mature interneuron clusters (Fig. 5c). We next performed deconvolution into four major
263 module eigengene (MEs), which revealed cell types classified as mature excitatory neurons
264 (turquoise and blue), microglia (brown), and unassigned (grey) (Fig. 5d). Quantification
265 supported enrichment in dividing radial glia, excitatory neurons, and microglia, the latter likely
266 driven by MCD candidate genes *IRF8* and *VSIG4* (Fig. 5e). Taken together, the expression of
267 MCD genes is more enriched in dorsal cortex neurogenic pools and implicated in the maturation
268 of excitatory rather than inhibitory neurogenic pools, as well as microglia.

269

270 **MCD gene expression is enriched in dysplastic cells**

271 We next performed differentially expressed gene (DEG) analysis in the MCD brain. We
272 reasoned that single-nucleus transcriptomes would be more revealing than bulk transcriptomes,
273 but the average VAF of ~6% in our MCD cohort meant that the vast majority of sequenced cells
274 would be genetically wild-type. We thus decided to focus snRNAseq on resected cortex from
275 patients with shared pathological MCD hallmarks but higher VAFs. We selected four resected
276 brain samples, two from patients with HME (HME-4688 *PIK3CA* p.E545K, 25.1% VAF and
277 HME-6593 *PIK3CA* p.H1047R, 13.1% VAF), and two from patients with TSC meet full
278 diagnostic criteria. We also included brains from four neurotypical cases as a comparison and
279 sequenced a total of 22,067 cells (see Methods).

280 While the TSC brain single nucleus transcriptomes showed substantial overlapping pools
281 with controls, HME brains showed a distinct UMAP distribution, located at the edges of the plot
282 (Fig. 6a). We found that very few HME cells matched expression patterns for typical brain cells,
283 even after standard normalization and scaling (Fig. 6b, Extended Data Fig. 5a, see Methods). We
284 thus labeled these clusters according to their closest relatives based upon established marker
285 gene expression in the control brain, labeled as ‘astrocyte-like (Ast-L)’ or ‘oligodendrocyte-like
286 (OD-L)’. Even with these categories, some clusters remained undefined (U) (Extended Data Fig.
287 5b,c). Interestingly, there was no single cell cluster that matched the VAF in the brain,
288 suggesting the mutant cells, as well as surrounding non-mutant cells, have dramatically disrupted
289 transcriptomes.

290 We noted that several of the HME clusters showed excessive expression of fibroblast
291 growth factor receptor (FGFR) gene families, specifically *FGFR1* in cluster U1/2 in HME,
292 *FGFR2/3* in cluster Ast-L1/3 and OD-L, *EGFR* in Ast-L1/3 and U1/2, and *PDGFRA* in cluster
293 U1/2 (Extended Data Fig. 5b,c). To identify the cell types expressing these genes, we performed
294 RNA in situ hybridization in HME brain sections followed by hematoxylin-eosin staining. We
295 found co-localization of these same *FGFR* family, *EGFR*, and *PDGFRA* transcripts with
296 dysplastic cells (Extended Data Fig. 6). Previous experiments suggest that it is most often the
297 dysplastic cells within HME and MCD that carry disease mutations⁷, suggesting an effect of
298 these mutations on growth factor receptor expressions that correlates with dysplasia.

299 Next, we investigated the expression patterns of MCD genes in this HME/TSC
300 snRNAseq dataset. An eigengene representing expression patterns of MCD genes was enriched
301 in Ast-L1/3 and OD-L, which were labeled as dysplastic cells (Fig. 6c). Interestingly, the
302 individual MCD genes displayed converging expression patterns resulting in six different
303 eigengenes (Fig. 6d, gene members for each eigengene are described in Extended Data Fig. 7)
304 which show distinct enrichment patterns across cell types (Fig. 6e), implying that membership of
305 each eigengene may be associated with the pathophysiology of the corresponding dysplastic cell
306 type in HMEs. We performed a pseudo-bulk DEG analysis comparing HME with CTRL and
307 detected 590 up-regulated genes and 1096 down-regulated genes. Intriguingly, 20% (15/75) of
308 MCD mutated genes in our list overlapped with DEGs of HME. Permutation testing suggests
309 that this overlap is unlikely to have arisen by chance (Fig. 6f, see Methods). Taken together,
310 many MCD genes are misregulated in MCD-specific cell types, suggesting that our MCD genes
311 may play important roles in the pathogenesis of dysplastic cells in MCDs.

312 313 **Discussion**

314 In this study, we use a multiomics approach to study the genetic landscape of MCD in the largest
315 reported cohort to date. We confirmed the important role of mTOR/MAP kinase and

316 glycosylation pathways, seen in about 60.5% of those with mutations. Moreover, our results also
317 linked novel biological processes including gene expression, synaptic function, calcium
318 dynamics, which made up the other 39.5% of mutations. Nevertheless, only 76 of 317 patients
319 showed one or more putative somatic mutations as a likely cause of MCD. There could be
320 numerous causes for the relatively low solve rate in MCD, including the potential to miss very
321 low VAF mutations and the contribution of complex mutations like structural variants or short
322 tandem repeats polymorphism. Finally, although patients with environmental causes, syndromic,
323 or inherited causes were excluded from our cohort, these factors could still contribute to MCD.

324 With our approach, we identified several recurrently-mutated genes not previously
325 implicated in MCD. Confirming the remaining candidate and identifying further MCD candidate
326 genes will require larger MCD cohorts. Including novel MCD candidate genes emerging from
327 300X WES into the 1000X Phase 3 AmpliSeq allowed both confirmation of mutations, a more
328 accurate estimate of VAF, and identification of additional patients with these genes mutated that
329 would have been perhaps missed with 300X WES. Functional validation by modeling mutations
330 in embryonic mouse brains suggests that most candidate genes we identified are likely to
331 contribute to disease. Perhaps it is not surprising that there are so many MCD genes, because
332 such mutations may avoid embryonic lethality due to their expression in just a small subset of
333 cells. Like with de novo germline mutations discovered in autism, we suggest that there could be
334 dozens if not hundreds of additional MCD genes, based in part upon the low number of
335 recurrently mutated genes⁴².

336 The four gene networks, mTOR/MAP kinase, calcium dynamics, synapse, and gene
337 expression, are intriguing, as they should play important roles of these genes both during brain
338 development and homeostasis. All four pathways are critical both for corticogenesis during
339 neurogenesis and neuronal migration, as well as neuronal excitability. For instance, calcium
340 dynamics is shown to regulate cytoskeletal activity and excitability^{43,44}. The genotypic
341 information also showed correlations with clinical features, for instance, PET brain
342 hypometabolism and abnormality in the neurological examination correlated with COSMIC DB
343 variants, opening the possibility to predict genotype based on phenotype.

344 We also characterized the expression patterns of MCD genes in the developmentally
345 normal and MCD brains at single-cell resolution. The cell types most strongly expressing
346 candidate MCD genes include dorsal forebrain radial glial progenitors and their daughter
347 excitatory neurons, as well as brain microglia, fitting well with the likely site of origin of somatic
348 brain mutations⁴⁵. Surprisingly, the dramatic gene dysregulation seen in the HME brain skewed
349 the UMAP plots in ways that could not be accounted for simply by the VAF. The fact that the
350 MCD genes also showed the strongest enrichment with these same clusters suggests that the
351 MCD genes are very likely to have pivotal roles in the HME condition. Prior studies on MCD
352 indicated that dysplastic cells express markers for both glia and neurons⁴⁶. Our findings,
353 however, suggest that MCD mutations drive critical roles predominantly in dividing radial glia,
354 with profound effects on lineage and cellular dysplasia. To conclude, the MCD genes in patient
355 brains found in our study demonstrated critical roles during cortical development, significantly
356 correlate with patient phenotypes, and could open doors to novel treatments for MCDs.

357

358 **Online Methods**

359

360 **Overview of the FCD cohort**

361 This study is a multi-center international collaboration. We recruited a cohort of 317 individuals
362 from ‘FCD Neurogenetics Consortium’ (see the member list). These individuals were diagnosed
363 with FCD type I, II, III, HME, or TSC and underwent surgical resection to treat drug-resistant
364 epilepsy between 2013-2021. Any case underwent surgical resection due to environmental
365 factors, for example stroke, acute trauma, were excluded. For each individual, resected brain
366 tissue was collected, along with paired blood or saliva samples and parental samples, where
367 available. Clinical history, pre- and post-operative brain imaging, histopathology, ILAE
368 classification according to surgical tissue pathology report, and Engel surgical outcome score (at
369 least two years after surgery) were collected, when available.

370

371 **Informed consent and study approval**

372 The study protocol was approved by the UC San Diego IRB (#140028). Informed consent was
373 obtained from all participants or their legal guardians at the time of enrollment.

374

375 **DNA extraction**

376 Pulverized cortical samples (~0.3 g) were homogenized with a Pellet Pestle Motor (Kimble,
377 #749540-0000) or Handheld Homogenizer Motor (Fisherbrand, #150) depending on the size of
378 the tissue, and resuspended with 450 µL RLT buffer (Qiagen, #40724) in a 1.5 ml
379 microcentrifuge tube (USA Scientific, #1615-5500). Homogenates were then vortexed for 1
380 minute and incubated at 70°C for 30 minutes. 50 µl Bond-Breaker TCEP solution (Thermo
381 Scientific, #77720) and 120 mg stainless steel beads with 0.2 mm diameter (Next Advance,
382 #SSB02) were added, and cellular disruption was performed for 5 minutes on a DisruptorGenie
383 (Scientific industries). The supernatant was transferred to a DNA Mini Column from an AllPrep
384 DNA/RNA Mini Kit (Qiagen, #80204) and centrifuged at 8500 xg for 30 seconds. The column
385 was then washed with Buffer AW1 (kit-supplied), centrifuged at 8500 xg for 30 seconds and
386 washed again with Buffer AW2 (kit-supplied), and then centrifuged at full speed for 2 minutes.
387 The DNA was eluted two times with 50 µl of pre-heated (70°C) EB (kit-supplied) through
388 centrifugation at 8,500 xg for 1 minute.

389

390 **MPAS and WES sequencing for somatic mutation candidates**

391 Massive parallel amplicon sequencing (MPAS) and whole-exome sequencing (WES) were used
392 at different phases to perform the genetic screening within available samples from the cohort.
393 Customized AmpliSeq DNA panels for Illumina (Illumina, #20020495) were used for Massive
394 Parallel Amplicon Sequencing¹⁷. 87 or 82 genes related to the mTOR pathway or curated based
395 on the results of Phase 1 and 2, respectively, were subjected to the AmpliSeq design system; a
396 list of designed genes is provided in Supplementary Table 2a-b. Two pools were designed for
397 tiling the capture region. Genomic DNA from extracted tissue was diluted to 5 ng/µL in low TE
398 provided in AmpliSeq Library PLUS (384 Reactions) kit (Illumina, #20019103). AmpliSeq was
399 carried out following the manufacturer's protocol (document #1000000036408v07). For
400 amplification, 14 cycles each with 8 minutes were used. After amplification and FUPA
401 treatment, libraries were barcoded with AmpliSeq CD Indexes (Illumina, #20031676) and pooled

402 with similar molecular numbers based on measurements made with a Qubit dsDNA High
403 Sensitivity kit (Thermo Fisher Scientific, #Q32854) and a plate reader (Eppendorf, PlateReader
404 AF2200). The pooled libraries were subjected to Illumina NovaSeq 6000 platform for PE150
405 sequencing. The AmpliSeq design in the ‘Phase 1’ is under the design ID IAA7610, and the
406 AmpliSeq design in ‘Phase 3’ is under the design ID IAA26010.

407 Genomic DNA (~ 1.0 µg) was prepared for whole-exome sequencing, and libraries were
408 captured using the Agilent SureSelect XT Human All Exon v.5 or Nextera DNA Exome kits.
409 Then, 100, 125, or 150 bp paired-end reads (median insert size ~ 210 bp) were generated using
410 the Illumina HiSeq X 2500 platform. The sequencing experiments were designed to yield three
411 datasets of ~ 100X coverage on each sample, with a coverage goal of 300X from the brain and
412 100X from blood/saliva.

413

414 **Somatic variant calling from MPAS and WES**

415 Reads were aligned to GRCh37 using BWA (version 3.7.16a), sorted per each read group, and
416 merged into a single BAM file with sambamba (version 0.6.7). The merged BAM files were
417 marked for duplicate reads using PICARD (v2.12.1), duplicated reads were not removed for
418 MPAS because of the nature of the method. Then, we performed indel realignment and base
419 quality recalibration using GATK (v3.7–0), resulting in the final uniformed processed BAM
420 files.

421 Both tissue-specific and tissue-shared mosaic variants were called from the MPAS and
422 WES sequencing data. MPAS and WES variants were called according to the availability of the
423 control tissue. Brain- and blood/saliva-specific variants were called using MuTect2 (GATK3.8)
424 paired mode and Strelka2 somatic mode⁴⁷; the BAM files from the brain sample (combined and
425 non-combined from independent sequencing libraries) and blood/saliva samples were treated as
426 “tumor-normal” and “normal-tumor” pairs separately and cross-compared between each other.
427 Variants called by both callers were listed. Mosaic variants shared between the brain and
428 fibroblast samples were called using the single mode of MosaicHunter¹¹ by either combining all
429 brain replicates or calling each separate sample. Variants that passed all the MosaicHunter filters
430 also were listed. Somatic variants from WES data were further called by GATK (v3.7–0)
431 haplotypcaller with ploidy parameter set to 50, followed by a series of heuristic filters described
432 as the best-practice by the Brain somatic mosaicism network¹², tissue-shared variants were called
433 by the combination of MuTect2⁴⁸ (GATK 3.8) single-mode and DeepMosaic¹⁰.

434 A union of different pipelines was selected to get maximum sensitivity. Mosaic
435 candidates from the combined lists were further filtered using the following criteria: (i) the
436 variant had more than 3 reads for the alternative allele; (ii) the variant was not present in UCSC
437 repeat masker or segmental duplications; (iii) the variant was at least 2 bp away from a
438 homopolymeric tract; and (iv) the variant exhibited a gnomAD allele frequency lower than
439 0.001. Variants that exist in the 1000 genome project (phase 3) also were excluded from the
440 analysis. Variants from both exome data sources were tested and a combination of tissue-specific
441 mosaic variants and tissue-shared mosaic variants were collected and the credible interval of
442 VAFs was calculated using a Bayesian-based method described previously⁴⁹. To filter for
443 candidate disease-causing variants for FCD, we further filtered out synonymous variants in
444 coding regions, variants with CADD Phred score < 25, and candidates that fell out of coding
445 regions and were not predicted to affect splicing by ANNOVAR.

446 **False discovery estimation**

447 To calculate false discovery of random variants detected in normal samples, we incorporated 75
448 normal control samples (71 brains and 4 other organs) previously sequenced with 250-300X
449 WGS, which should provide similar sensitivity as our exomes, the deep WGS were generated by
450 efforts from the NIMH Brain Somatic Mosaicism Consortium¹², from controls¹⁷, and from our
451 recent mutation detection pipeline¹⁸. Variants were filtered based on the identical criteria as
452 described in the above data analysis part, with >0.01 VAF, all on exonic regions defined by
453 NCBI, and CADD score >25. While 13 variants remain positive from this pipeline from the 75
454 samples (0.17 per control), 306 candidate variants were determined in our 134 MCD exomes
455 (2.28 per MCD case), which lead to an estimated 7.59% per sample false discovery rate
456 (Supplementary Table 5).

457 **Orthogonal validation and quantification of mosaic mutations with targeted amplicon** 458 **sequencing**

459 Targeted amplicon sequencing (TASeq) with Illumina TruSeq was performed with a coverage
460 goal of >1000X for 554 candidate variants detected by computational pipelines described above
461 for both MPAS and WES, to experimentally validate the mosaic candidates before functional
462 assessment. PCR products for sequencing were designed with a target length of 160-190 bp with
463 primers being at least 60 bp away from the base of interest. Primers were designed using the
464 command-line tool of Primer3^{50,51} with a Python (v3.7.3) wrapper^{13,14}. PCR was performed
465 according to standard procedures using GoTaq Colorless Master Mix (Promega, M7832) on
466 sperm, blood, and an unrelated control. Amplicons were enzymatically cleaned with ExoI (NEB,
467 M0293S) and SAP (NEB, M0371S) treatment. Following normalization with the Qubit HS Kit
468 (ThermoFisher Scientific, Q33231), amplification products were processed according to the
469 manufacturer's protocol with AMPure XP beads (Beckman Coulter, A63882) at a ratio of 1.2x.
470 Library preparation was performed according to the manufacturer's protocol using a Kapa Hyper
471 Prep Kit (Kapa Biosystems, KK8501) and barcoded independently with unique dual indexes
472 (IDT for Illumina, 20022370). The libraries were sequenced on Illumina HiSeq 4000 or NovaSeq
473 6000 platform with 100 bp paired-end reads.

474

475 **Mutational signature analysis**

476 Mutational signature analysis was performed using a web-based somatic mutation analysis
477 toolkit (Mutalisk)⁵². PCAWG SigProfiler full screening model was used.

478

479 **STRING analysis**

480 STRING analysis was performed by STRING v11²². A total of 75 MCD genes were loaded as
481 input and MCL clustering was performed. The terms in Gene Ontology (GO), KEGG pathways,
482 Top 10 terms GO or KEGG pathways were shown in Fig. 2b. If there are less than 10 terms for
483 those terms (such as clusters 3 and 4 in Fig. 2), we included all the terms in GO or KEGG
484 pathways, Local network cluster (STRING), Reactome pathways, and Disease-gene associations
485 (DISEASES) to show the enriched terms. Visualization was performed by Cytoscape v3.9.

486

487 **ClueGO**

488 Visualization of the functionally grouped biological terms was performed by ClueGO v2.5⁵³, a
489 Cytoscape plug-in. A total of 75 MCD genes from Fig. 2 were loaded and GO terms in the
490 'Biological Process' category were used for visualization. Terms with a $p < 0.01$, a minimum
491 count of 3, and an enrichment factor > 1.5 , are grouped into clusters based on membership
492 similarities.

493

494 **Animals**

495 Pregnant Crl: CD1(ICR) mice for mouse modeling were purchased from Charles River
496 Laboratory. All mice used were maintained under standard group housing laboratory conditions
497 with 12 hours light/dark cycle and free access to food and water. The age and number of mice
498 used for each experiment are detailed in the figure legends. The sex of the embryos used was not
499 tested. All work with mice was performed in accordance with UCSD IACUC protocol S15113.

500

501 **DNA constructs**

502 *RRAGA*, *KLHL22*, and *RHOA* ORF regions were amplified from the hORFeome library and
503 inserted into the pCIG2 (pCAG-IRES-GFP) vector. *GRIN2C* ORF region was purchased from
504 DNASU Plasmid Repository in Arizona State University Biodesign Institute. All sequences of
505 clones were confirmed by sanger sequencing.

506

507 **In utero electroporation**

508 In utero electroporation was performed as described previously⁵⁴ with modifications as follows.
509 Endotoxin-free plasmids (0.5–1 μg) plus 0.1% Fast Green (Sigma, catalog no. 7252) was injected
510 into one lateral ventricle of E14.5 embryos. Electroporation was performed by placing the anode
511 on the side of the DNA injection and the cathode on the other side of the head to target cortical
512 progenitors. Four pulses of 45 V for 50 ms with 455-ms intervals were used.

513

514 **Mouse brain section preparation**

515 An E18 mouse brain is fixed in 4% paraformaldehyde (PFA) for 2 hrs. For the P21 mouse brain,
516 a mouse was anesthetized by isoflurane and perfused by cold 1X PBS for 8 min and following
517 4% cold PFA for 8 min. The brains were dehydrated in 30% sucrose in 1x PBS for 48 hrs and
518 embedded in Tissue-Tek optimal cutting temperature compound and frozen on dry ice. A frozen
519 block was sectioned with 20 μm thickness in a cryostat (CryoStar NX70, Thermo Fisher
520 Scientific) and placed on sliding glass. The attached sections were dried on a 50 °C heating block
521 for 3 hrs.

522

523 **Immunofluorescence staining and imaging**

524 A section was rehydrated and washed by 1X PBS for 10 min 3 times, permeabilized in PBST
525 (0.3% Triton X-100 in 1X PBS) for 10 min, and blocked by blocking solution (5% normal BSA
526 in 1X PBS) for 2 hrs in room temperature. Sections were stained with diluted primary antibodies
527 in the blocking solution overnight at 4 °C. The next day, the sections were washed with PBST for
528 5 min three times and stained with secondary antibodies in blocking solution for 2 hrs in RT.
529 Blocking solution was dropped off from the slides and nuclei staining with DAPI solution
530 (0.1 $\mu\text{g}/\text{ml}$ of DAPI in PBST) was performed for 15 min. The slides were mounted with DAKO

531 fluorescent mount solution (catalog no. S3023). Zeiss 880 Airyscan Confocal is used for imaging
532 according to the manufacturer's instructions.

533

534 **Antibodies**

535 phospho-S6 (1:800 dilution, catalog no. 5364S ;Cell Signaling, AB_10694233), NeuN (1:100,
536 MAB377X; Sigma-Aldrich, AB_2149209), GFP (1:500, catalog no. GFP-1020, Aves Labs,
537 AB_10000240), Alexa Fluor Goat 488 chicken IgY (H+L) (1:1,000 dilution, catalog no. A-
538 11039, AB_2534096), Alexa Fluor 594 donkey anti-rabbit IgG (H+L) (1:1,000, catalog no.
539 R37119, AB_2556547).

540

541 **Genotype-phenotype association**

542 The functional modules to be tested were selected based on the enriched GO terms (Fig. 2 and
543 Extended Data Fig. 4). A given candidate MCD gene was assigned as a member to one or
544 multiple modules based on GO terms related to the given gene (results summarized in
545 Supplementary Table 3c). Subsequently, a given patient became a member of one (or multiple)
546 functional module(s) if the genes detected in that patient was assigned to that (those) functional
547 module(s). All available clinical information on the patient was collected and harmonized using
548 ILAE terms (summarized in Supplementary Table 4). Pearson correlation coefficients were
549 calculated by `cor.test()` function in R. The value of correlation coefficients were displayed as
550 colors in heatmap of Fig. 4. If two groups with binary values were used for calculation, Phi
551 coefficient was used.

552

553 **Single-nucleus RNA sequencing**

554 A fresh-frozen brain tissue (~50 mg) was placed into a glass dounce homogenizer containing 1
555 ml cold lysis buffer (0.05 % (v/v) NP-40, 10 mM Tris (pH 7.4), 3 mM MgCl₂, 10 mM NaCl) and
556 dounce 10 times with a loose pestle and following 10 times with a tight pestle. The homogenate
557 was incubated for 10 min in RT. 9 ml of wash buffer (1% BSA in 1X PBS) was added to the
558 homogenate and filtered by a 30 um cell strainer. The strained homogenate was spun down in
559 500 g to remove the supernatant. The pellet was resuspended by 5 ml of wash buffer. Straining,
560 spinning down steps was performed once more, and the pellet was resuspended into 500 ul of
561 wash buffer. 10 ul of nuclei resuspension was mixed with counting solution (0.02 % Tween 20,
562 0.1ug/ml DAPI, 1% BSA in 1X PBS) and nuclei density was measured by manual nuclei
563 counting using DAPI signal. The resuspension was diluted by wash buffer to make the desired
564 concentration (800~1000 nuclei/ul). 1~4 samples were pooled together targeting 10000 nuclei
565 per reaction. Gel beads emulsion (GEM) generation, cDNA, and sequencing library
566 constructions were performed in accordance with instructions in Chromium Single Cell 3'
567 Reagent Kits User Guide (v3.1). A library pool was sequenced with 800 million read pairs using
568 NovaSeq 6000.

569

570 **Single-nucleus RNAseq bioinformatics pipeline**

571 Fastq files from single-nucleus libraries were processed through Cell Ranger (v6.0.2) analysis
572 pipeline with `--include-introns` option and hg19 reference genome. Pooled library was
573 demultiplexed and singlets were taken by demuxlet. Seurat (v4) package was used to handle

574 single nuclei data objects. Protein coding genes were used for further downstream analysis.
575 Nuclei passed a control filter (number of genes > 500, number of reads >1000, percentage of
576 mitochondrial gene < 10%) was used for downstream analysis. Data were normalized and scaled
577 with the most variable 5000 features using the ‘NormalizeData’ and ‘ScaleData’ functions.
578 Dimensionality reduction by PCA and UMAP embedding was performed using runPCA and
579 runUMAP function. Clustering was performed by FindNeighbors and FindClusters function. Cell
580 type identification was performed using known cell type markers expressed in the brain
581 including excitatory/inhibitory neuron, astrocyte, oligodendrocyte, microglia, and endothelial
582 cell markers as well as using positive markers found by FindAllMarkers function with 3000 most
583 variable features in scaled data.

584

585 **Weighted gene co-expression network analysis**

586 ‘r-wgcna’ package (v1.69) was used for WGCNA according to instructions (PMID: 19114008).
587 Briefly, a similarity matrix was generated based on Pearson’s correlation coefficient value
588 among the top 3000 variable features in single-nucleus transcriptome data, which was used to
589 calculate the subsequently signed type of network adjacency matrix. Next, the topological
590 overlap matrix (TOM) and the corresponding dissimilarity (1-TOM) value were generated from
591 the adjacency matrix. Finally gene modules were generated by ‘cutreeDynamic’ function with
592 ‘tree’ method, minAbsSplitHeight = 0.9 and minClusterSize = 30 option. Similar gene modules
593 were merged by ‘mergeCloseModules’ function with cutHeight = 0.25. String analysis was
594 performed using each gene module for the identification of the given module’s functional
595 characteristics.

596

597 **RNAscope**

598 We used published methods and purchased target probes for genes of interest containing an 18-
599 25 base region complementary to the target, as spacer sequencing, and a 14 base Z-tail
600 sequence⁵⁵, including RNA pol III positive control and random sequence negative control,
601 following the manufacturer recommendations (Advanced Cell Diagnostics, Hayward, CA).
602 Images were acquired on a Leica STED Sp8 with Falcon microscope.

603

604 **Permutation analysis for the enrichment of MCD genes**

605 To test the enrichment of differentially expressed MCD genes in RNA sequencing against a
606 random distribution, we designed a permutation analysis. All human genes used in the single-cell
607 RNA-seq analysis (n=19909) were randomly shuffled 10,000 times and the same number of
608 genes as described in the differential expression analysis (n=1686) was selected for each shuffle.
609 The number of overlaps between each shuffle and the MCD candidates was compared and the
610 number of overlaps was used as the outcome and a null distribution was generated from the
611 10,000 shuffles. All 75 positively validated MCD genes are confirmed to be existing in the initial
612 gene list. After 10,000 permutations, the permutation p-value was calculated with numbers >=
613 observed overlap (p=0.0017 for the data shown in the main text).

614

615 **Statistical analyses**

616 Statistical analyses were performed by R or Prism 8 (GraphPad Software). Two-way ANOVA
617 and Sidak multiple comparisons were performed in Fig 3b with p-values of interaction between
618 genotype and bin factor. **** $p < 0.0001$, *** $p < 0.001$, ** $p < 0.01$, * $p < 0.05$.

619

620 **Code and data availability**

621 Code to generate the figures and analyze the data are publically available on GitHub
622 (https://github.com/shishenyxx/MCD_mosaic). WES and AmpliSeq data are deployed on NIMH
623 Data Archive under study number 1484 “Comprehensive multiomic profiling of somatic
624 mutations in malformations of cortical development” and SRA under accession number
625 PRJNA821916: “Comprehensive multiomic profiling of somatic mutations in malformations of
626 cortical development”. The snRNAseq R object was deposited in Single Cell Portal
627 ([https://singlecell.broadinstitute.org/single_cell/study/SCP1815/comprehensive-multiomic-](https://singlecell.broadinstitute.org/single_cell/study/SCP1815/comprehensive-multiomic-profiling-of-somatic-mutations-in-malformations-of-cortical-development#study-download)
628 [profiling-of-somatic-mutations-in-malformations-of-cortical-development#study-download](https://singlecell.broadinstitute.org/single_cell/study/SCP1815/comprehensive-multiomic-profiling-of-somatic-mutations-in-malformations-of-cortical-development#study-download)).

629

630 **Acknowledgments**

631 AmpliSeq, TASEq, and snRNAseq were supported by NIH P30CA023100 and S10OD026929 at
632 the UCSD IGM Genomics Center. Rady Children’s Institute for Genomic Medicine, Broad
633 Institute (U54HG003067, UM1HG008900), the Yale Center for Mendelian Disorders
634 (U54HG006504), and the New York Genome Center provided whole-exome sequencing. UCSD
635 Microscopy core (NINDS P30NS047101) provided imaging support. CC was supported by a
636 2021 Brain & Behavior Research Foundation Young Investigator Grant. This study was
637 supported by the NIH (NIMH U01MH108898 and R01MH124890 to JGG and GWM, and NIA
638 R21AG070462, NINDS R01NS083823 to JGG). We thank St éphanie Baulac and Sara
639 Baldassari for sharing unpublished exome data.

640

641 **Author contributions**

642 C.C., X.Y., and J.G.G. designed the study. C.C., S.M., and S.K. conducted functional validation.
643 C.B., V.S., A.N., E.R., C.C., and G.H. coordinated the clinical database. X.Y., C.C., M.W.B.,
644 L.L.B., R.D.G., J.G., M.X., A.P.L.M., and K.N.J. organized, handled, and sequenced human
645 samples. X.Y., C.C., T.B., X.X., and B.C. performed bioinformatics and data analysis. C.C. and
646 K.I.V. performed the RNAscope experiment. C.D., H.W.P., C.A.B.G., S.H.K., H.K., A.S.,
647 C.A.H., C.G., C.A.G., S.S., M.N., D.D.G., K.I., Y.T., R.C., J.T., V.C., R.G., O.D., W.A.S.,
648 H.R.M., and G.W.M. provided resected brain tissues and clinical data from FCD patients. C.C.,
649 X.Y., and J.G.G. wrote the manuscript. All authors read and commented on the manuscript
650 before submission.

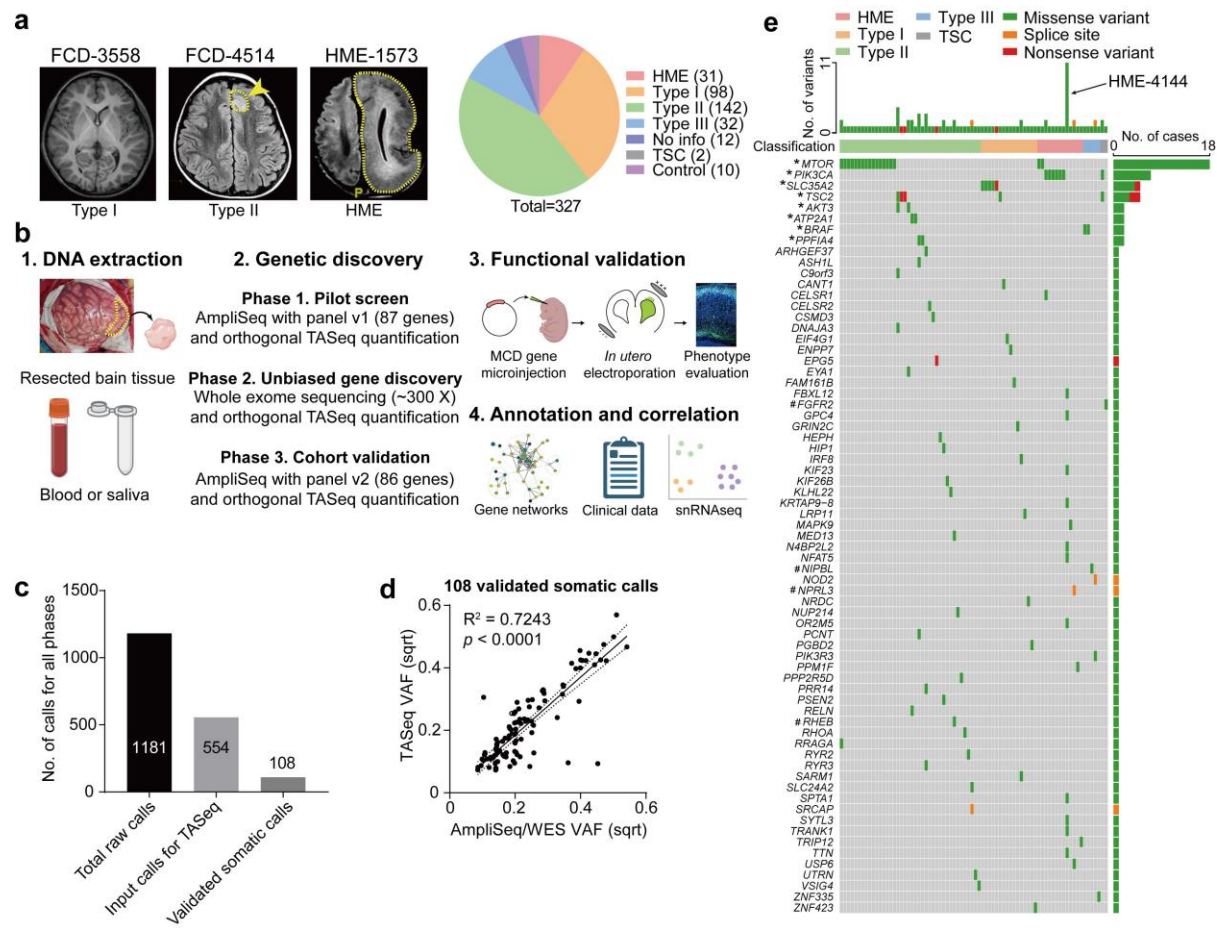
651

652 **Competing Interests Statement**

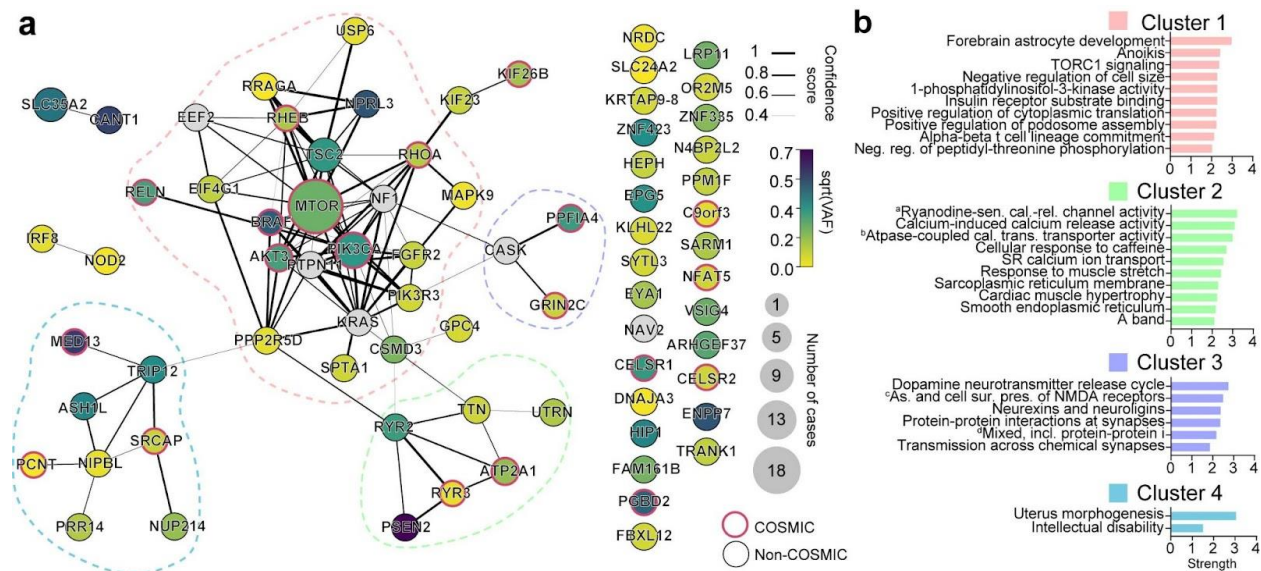
653 The authors declare no competing interests.

654

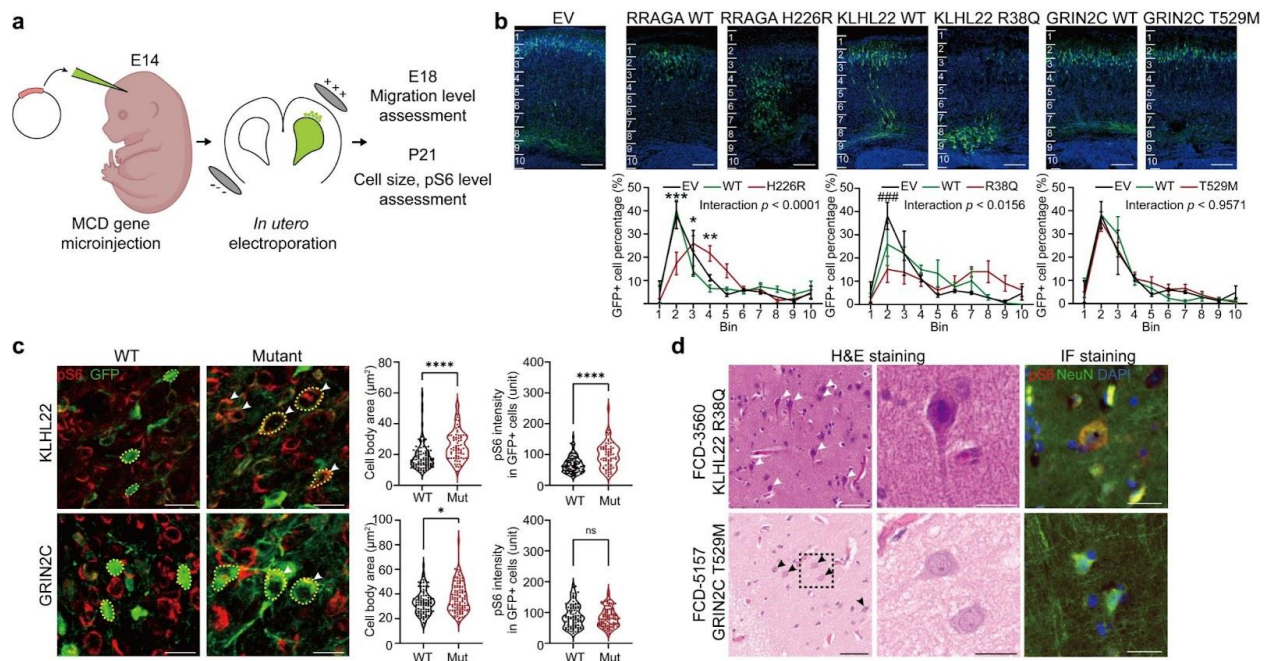
655



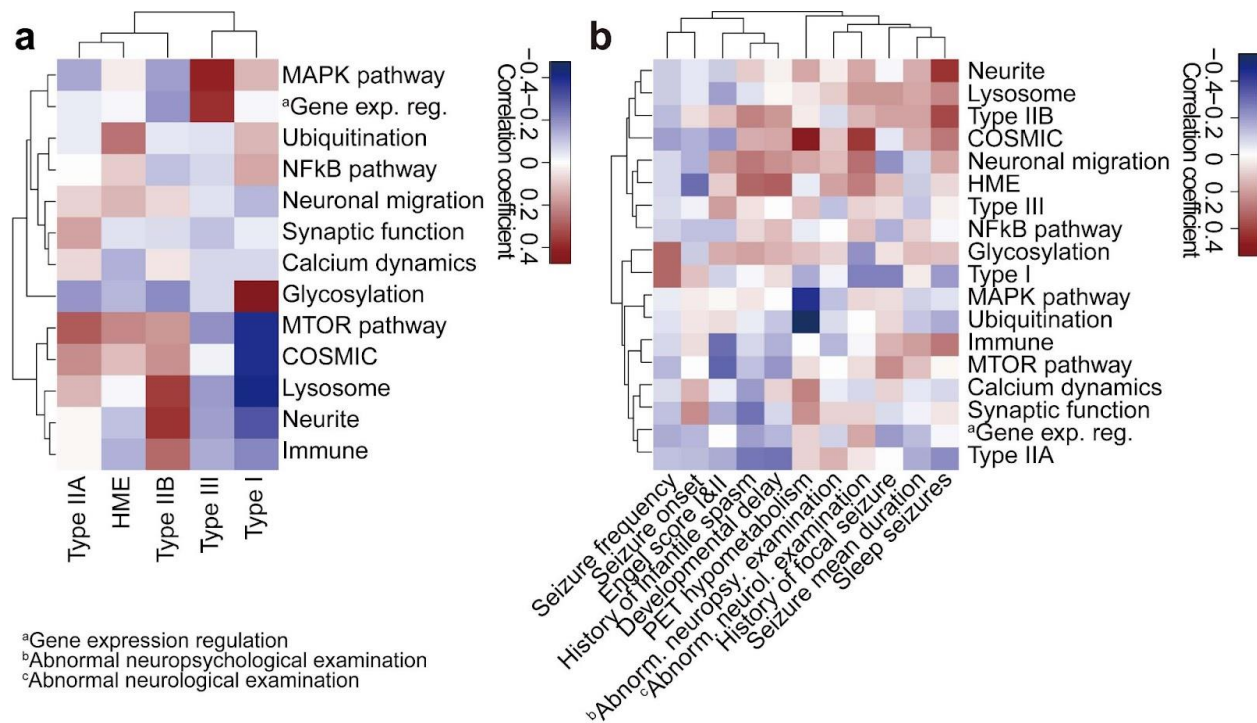
656
 657 **Figure 1. Comprehensive genetic profiling and validation of somatic variants in 327 MCD**
 658 **patients.** (a) Representative MRI image of FCD-3588 (FCD type I), FCD-4514 (FCD type II),
 659 HME-1573, and a pie chart for the composition of our MCD cohort. Yellow arrow and dash:
 660 affected brain regions. (b) Workflow for comprehensive genetic profiling of MCD, using a three-
 661 phase approach from patient DNA. Each phase was followed by quantification/validation of each
 662 variant with target amplicon sequencing (TASEq). Phase 1] 1000 × pilot screening of DNA with
 663 an 87-gene mTOR-related panel. Phase 2] 300 × whole-exome sequencing (WES) with and best-
 664 practice somatic variant discovery for novel candidate discovery. Phase 3] Cohort-level
 665 validation with an updated, high-confidence TASEq gene set based on knowledge from Phase 1
 666 and 2. A subset of the somatic mutations was further functionally validated by mouse modeling.
 667 Candidate genes were annotated and correlated with external datasets such as STRING DB,
 668 clinical phenotype dataset, and newly generated single-nucleus RNAseq dataset from MCD
 669 brain. (c) Somatic variant calls were detected from all three phases of genetic discovery, yielding
 670 108 validated somatic calls. (d) Correlation between square-root transformed (sqrt)
 671 AmpliSeq/WES variant allele fraction (VAF) and TASEq VAF. Solid line: best-fit line linear
 672 regression. Dotted lines: 95 % confidence band of the best-fit line. (e) Oncoplot with all 69
 673 validated somatic SNVs from this study. Top: most patients had one gene mutated, a few patients
 674 had more than one gene mutated, and patient HME-4144 had 11 different validated gene
 675 mutations. Color: type of variant. * and #: recurrent genes in our cohort, and non-recurrent in our
 676 cohort but recurrent in other studies, respectively.



677
 678 **Figure 2. Four major gene networks were discovered from the comprehensive MCD gene**
 679 **profiling.** (a) STRING DB pathway analysis of the 69 MCD discovered genes and six novel
 680 genes from recent publications identifies MTOR/MAP kinase pathway (pink, Cluster 1),
 681 Calcium dynamics (green, Cluster 2), Synapse (purple, Cluster 3), Gene expression (blue,
 682 Cluster 4). Edge thickness: confidence score calculated by STRING. Size and color of a node:
 683 square root transformed ($\sqrt{\text{VAF}}$) number of patients carrying a given mutation and average $\sqrt{\text{VAF}}$
 684 across all patients, respectively. Non-clustered orphan genes are listed on the right. Red
 685 border: variant reported in the COSMIC database. (b) Gene Ontology (GO) analysis results
 686 confirmed the functions of compositions in each network. Top GO terms or KEGG pathways.
 687 Strength calculated by STRING.
 688

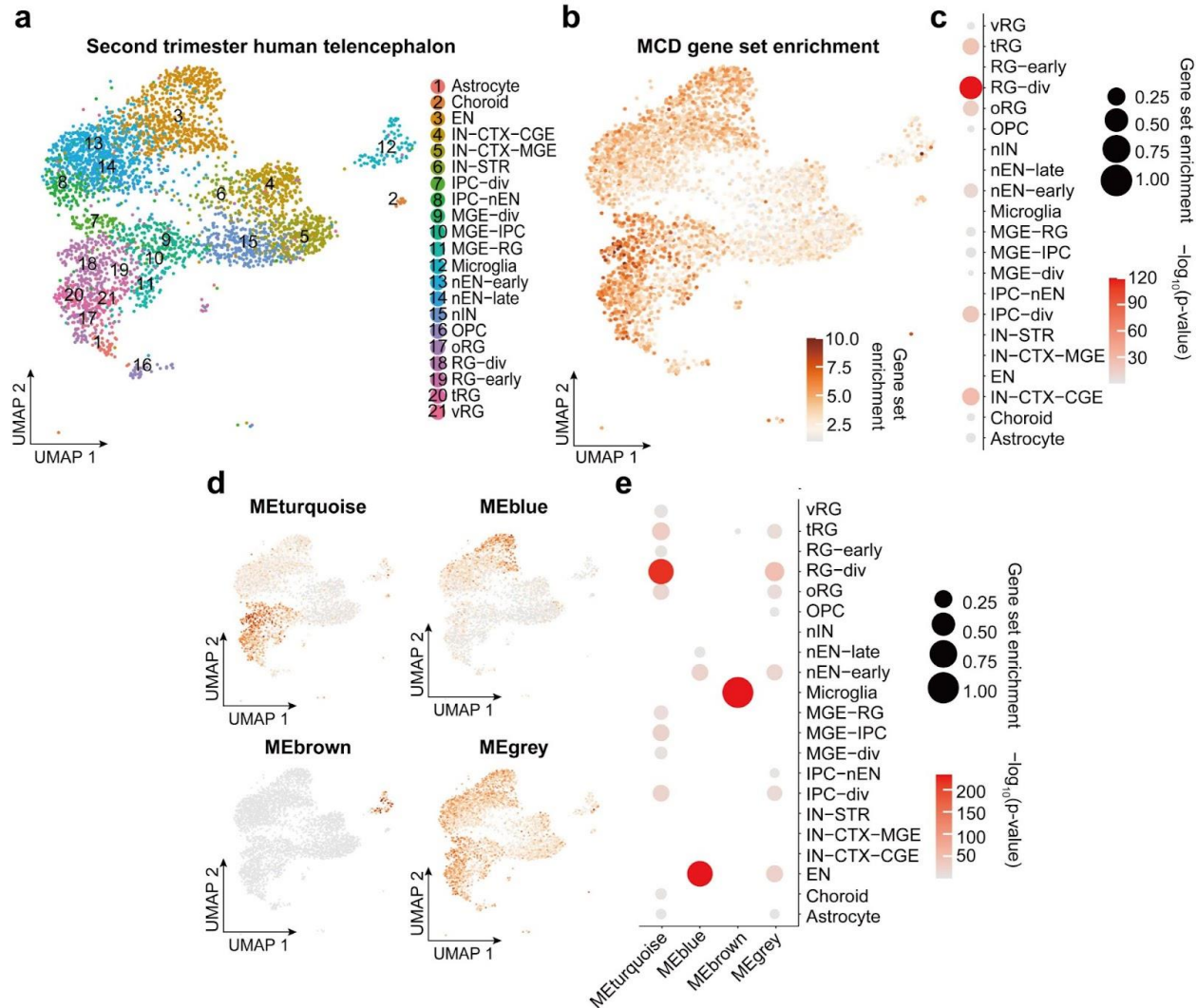


689
 690 **Figure 3. Selected novel MCD somatic variants show functional defects in embryonic**
 691 **mouse brain and patient samples.** (a) Workflow for functional validation of candidate mosaic
 692 variants in mice. (b) Two different mutations in novel FCD type II genes, *RRAGA* H226R and
 693 *KLHL22* R38Q, but not a novel FCD type I gene, *GRIN2C*, disrupt cellular radial migration from
 694 the subventricular zone (SVZ). Below: two-way ANOVA and Sidak multiple comparisons with
 695 *p*-values of interaction between genotype and bin factor. * or # indicates a *p*-value in comparison
 696 between WT and mutant group, or EV and mutant group respectively. Ten bins from the surface
 697 of the cortex (top) to SVZ (bottom). Scale bar: 100 μm . Error bar: $\pm\text{SE}$. (c) Immunofluorescence
 698 in postnatal day 21 mouse cortices for *KLHL22* and *GRIN2C* wild-type (WT) or mutant isoform.
 699 Neurons expressing mutant *KLHL22* and *GRIN2C* recapitulate histological phenotypes shown in
 700 (d), with enlarged cell bodies (white arrow) compared to WT isoforms (WT control), whereas
 701 only neurons expressing *KLHL22* but not *GRIN2C* mutant isoform display increased pS6 levels
 702 compared to control. Dotted lines: examples of cell body size quantification. Two-sided
 703 Student's *t*-test. Scale bar: 20 μm . (d) H&E and phospho-S6 (pS6) staining of the resected brain
 704 from FCD-3560 and FCD-5157. Box area is zoomed in the middle image. Arrows: dysplastic
 705 cells. Right: Immunofluorescence (IF) for pS6 and NeuN. Note dysplastic pS6-positive neurons
 706 with increased pS6 level are present in FCD-3560 but not in FCD-5157. Scale bar: 60 μm at left,
 707 20 μm on middle and right. **** $p < 0.0001$; * $p < 0.05$; ns, non-significant. ### $p < 0.001$. EV:
 708 empty vector.



709
 710 **Figure 4. Clinical phenotypic outcomes correlate with genotype-based classifications in**
 711 **MCD.** (a) Correlation heatmap for classification based on genetic information (y-axis) vs.
 712 International League Against Epilepsy (ILAE) classification based on histology (x-axis) using
 713 Pearson correlation. Shade: value of Phi coefficient. Note Type IIA and HME are enriched with
 714 mTOR and Ubiquitination genes, while Type I is enriched in Glycosylation and depleted in
 715 MTOR and COSMIC genes. HME: hemimegalencephaly. (b) Correlation between classification
 716 based on genetic information and various clinical phenotypes. Shade: value of Phi (binary data)
 717 or Pearson (continuous) correlation coefficient. For example, positron emission tomography
 718 (PET) hypometabolism is enriched in COSMIC genes and depleted in MAPK pathway, whereas
 719 abnormal neurological examination is enriched in COSMIC genes. The whole dataset is in
 720 Supplementary table 4.

721



722

723

724 **Figure 5. Single-nucleus transcriptomes reveal MCD gene enrichment in radial glia and**

725 **excitatory neurons in the developing human cortex.** (a) Uniform Manifold Approximation and

726 **Projection (UMAP) for single-nucleus transcriptome in 2nd trimester fetal human telencephalon**

727 **from a public dataset⁴¹. (b) UMAP enrichment patterns of an eigengene using MCD genes. Note**

728 **enrichment for excitatory neurons and radial glia (dark brown). vRG: vertical radial glia, tRG:**

729 **truncated radial glia, RG-div: dividing radial glia, oRG: outer radial glia, EN: excitatory neuron,**

730 **nEN: newborn excitatory neuron, IPC: intermediate progenitor cell, STR: striatum, IN:**

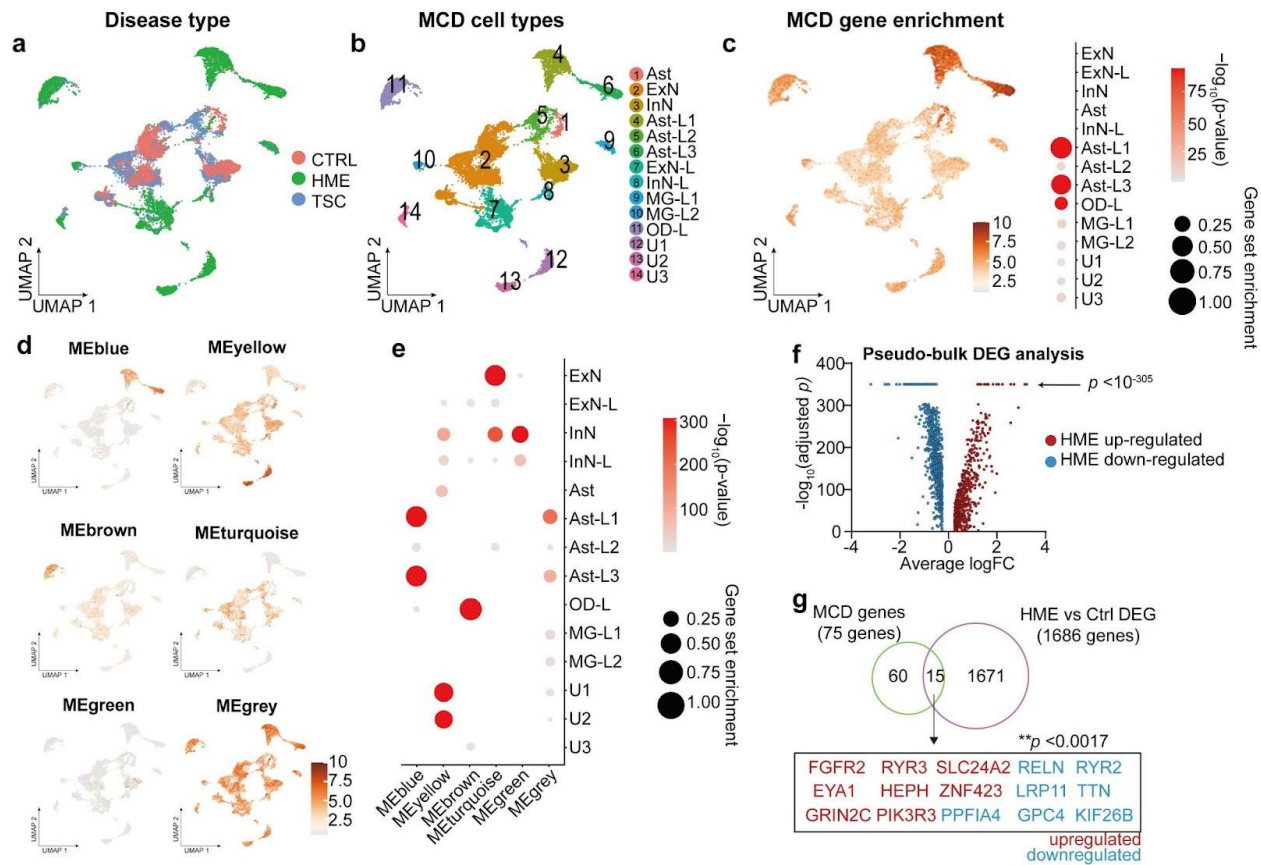
731 **interneuron, CTX: cortex, MGE: medial ganglionic eminence, CGE: central ganglionic**

732 **eminence. (c) Quantification of enrichment of (b) based on cell types, showing enrichment for**

733 **RG-div. (d) Four eigengenes decomposed from (b). (e) Quantification of enrichment of (d) based**

734 **on cell types showing enrichment in dividing radial glia, microglia and inhibitory cortical**

735 **neurons from the medial ganglionic eminence (MGE).**



735

736

737

738

739 **Figure 6. Single-nucleus transcriptomes showed MCD gene expression enriched in MCD-**
 740 **specific cell types.** (a) UMAP for single-nucleus transcriptome of 22067 nuclei from the cortical
 741 lesions of control (CTRL), hemimegalencephaly (HME), and tuberous sclerosis complex (TSC)
 742 brain. (b) Cell type classification. Ast: astrocyte, ExN: excitatory neuron, InN: inhibitory neuron,
 743 MG: microglia, OD: oligodendrocyte, U: unidentified. (c) The expression pattern of an
 744 eigengene made with all MCD genes and the quantification of enrichment based on cell types.
 745 (d) Six eigengenes decomposed from (c). (e) Quantification of the cell-type-specific enrichment
 746 in (d). (f) A volcano plot from DEG list of HME versus CTRL pseudo-bulk data. The genes
 747 having adjusted $p < 10^{-305}$ were pointed by arrow. (g) The MCD genes overlapping with DEGs of
 748 HME in contrast to controls. Permutation test (10,000 times) shows a very rare chance ($p <$
 749 0.0017) to show this overlap in a random sampling of 1686 genes from 19909 protein-coding
 750 genes used in these DEGs. Red or blue coloring of gene names indicates upregulated or
 751 downregulated DEGs in HMEs compared to CTRLs, respectively.

752

753 **Supplementary Table Descriptions**

754 **Supplementary Table 1. The cohort list and corresponding sequencing methods.** The 327
755 cases are listed in each row and corresponding sequencing methods used for a given sample was
756 described.

757
758 **Supplementary Table 2. AmpliSeq primer pool designs** (a) Ampliseq primer pool design used
759 in phase 1. (b) Ampliseq primer pool design used in phase 3.

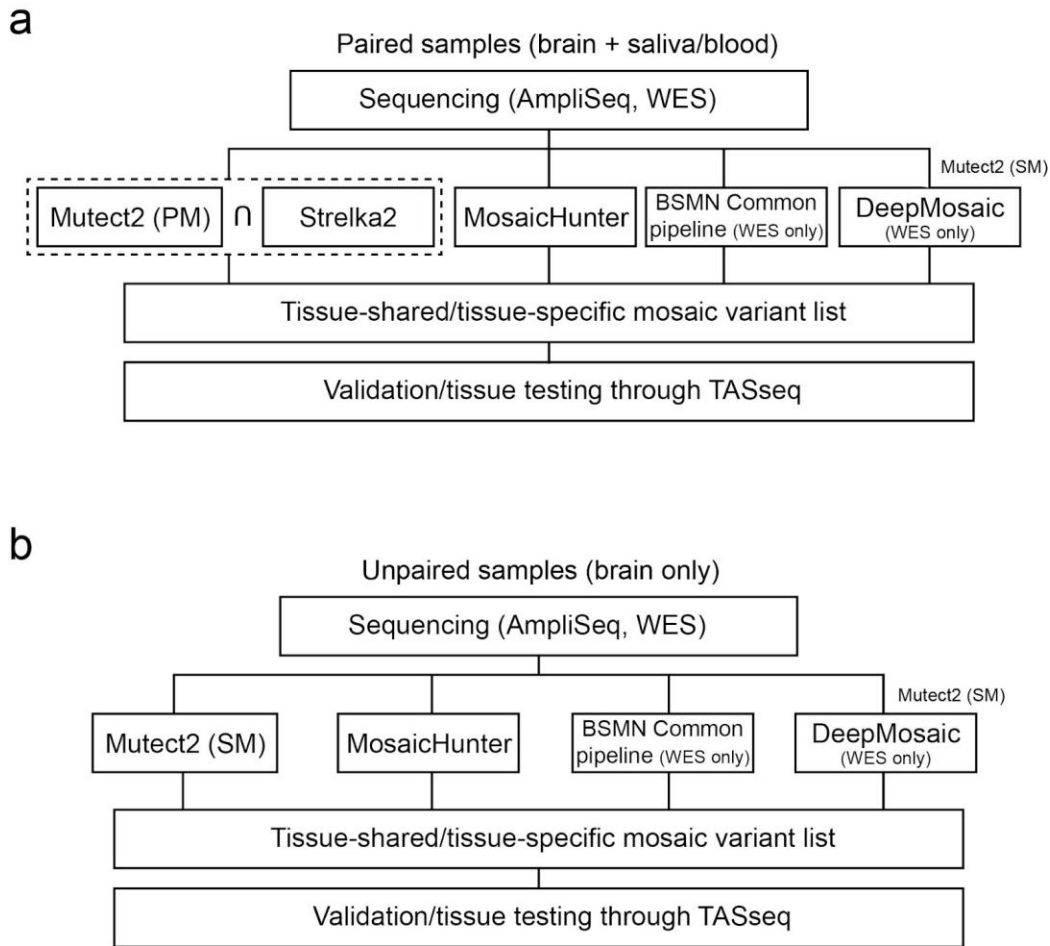
760
761 **Supplementary Table 3. The summary of SNV calls across the three phases of genetic
762 discovery.** (a) 1811 raw calls derived from the combination of variant callers described in
763 Extended Data Fig. 1. (b) 554 input SNV calls participated in TASEq quantification. (c)
764 Validated brain somatic SNV calls from (b). (d) Annotation table of the genes listed in (c) based
765 on GO terms.

766
767 **Supplementary Table 4. The summary of phenotype and genotype information for the
768 ‘genetically solved’ cases.**

769
770 **Supplementary Table 5. The summary table used for false discovery estimation.**

771

772



773

774

775 **Extended Data Fig. 1 Bioinformatic pipeline to detect somatic SNVs in the MCD cohort. (a)**

776 The pipeline for paired samples. Notably, the dashed square indicates that the sharing variants

777 between MuTect2 paired mode and Strelka2 were used for the downstream analysis. BSMN

778 common pipeline and DeepMosaic were used only for WES datasets. The DeepMosaic input

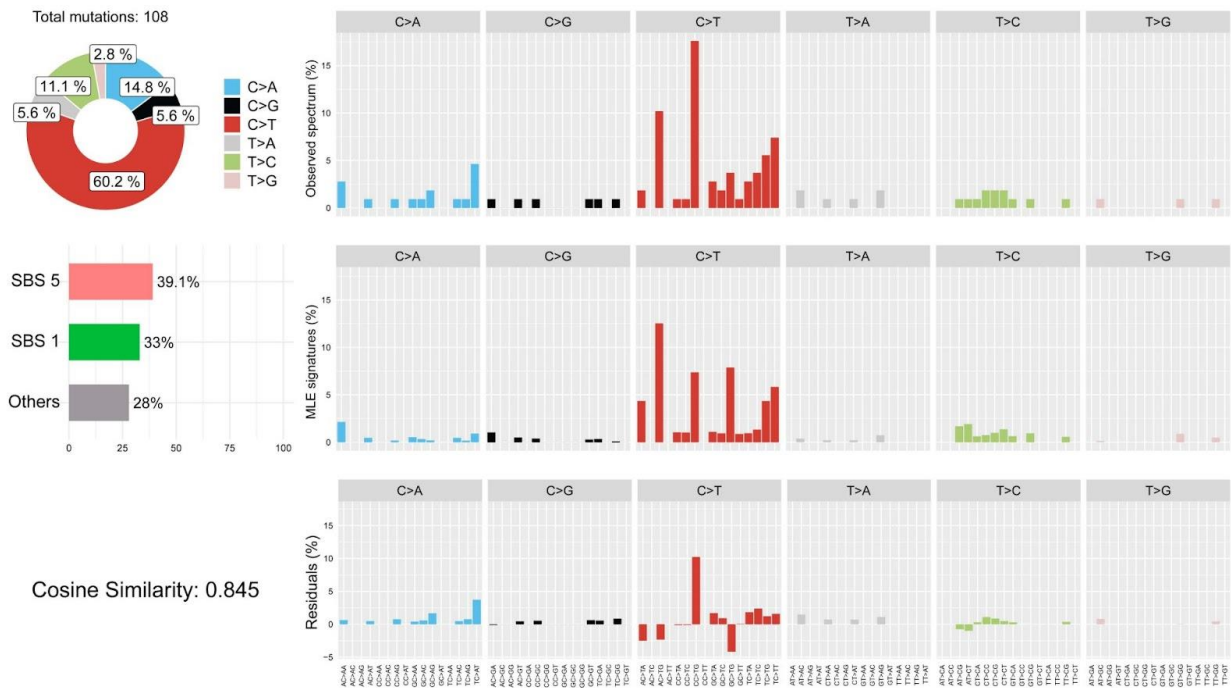
779 variants were generated by MuTect2 single mode. (b) The pipeline for unpaired samples. The

780 pipeline is similar except that MuTect2 single mode without Strelka2 is used. PM: paired mode,

781 SM: single mode.

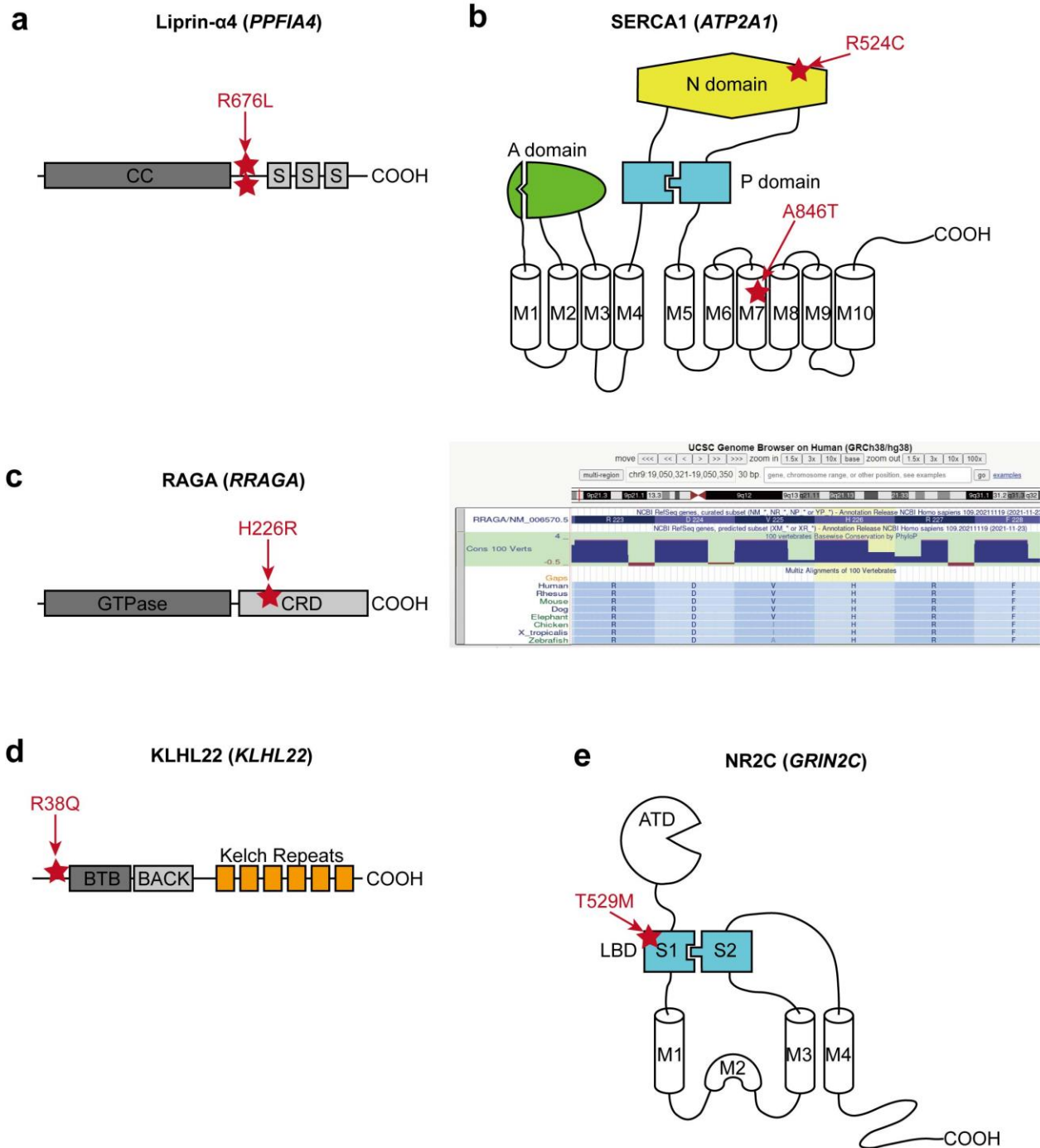
782

783



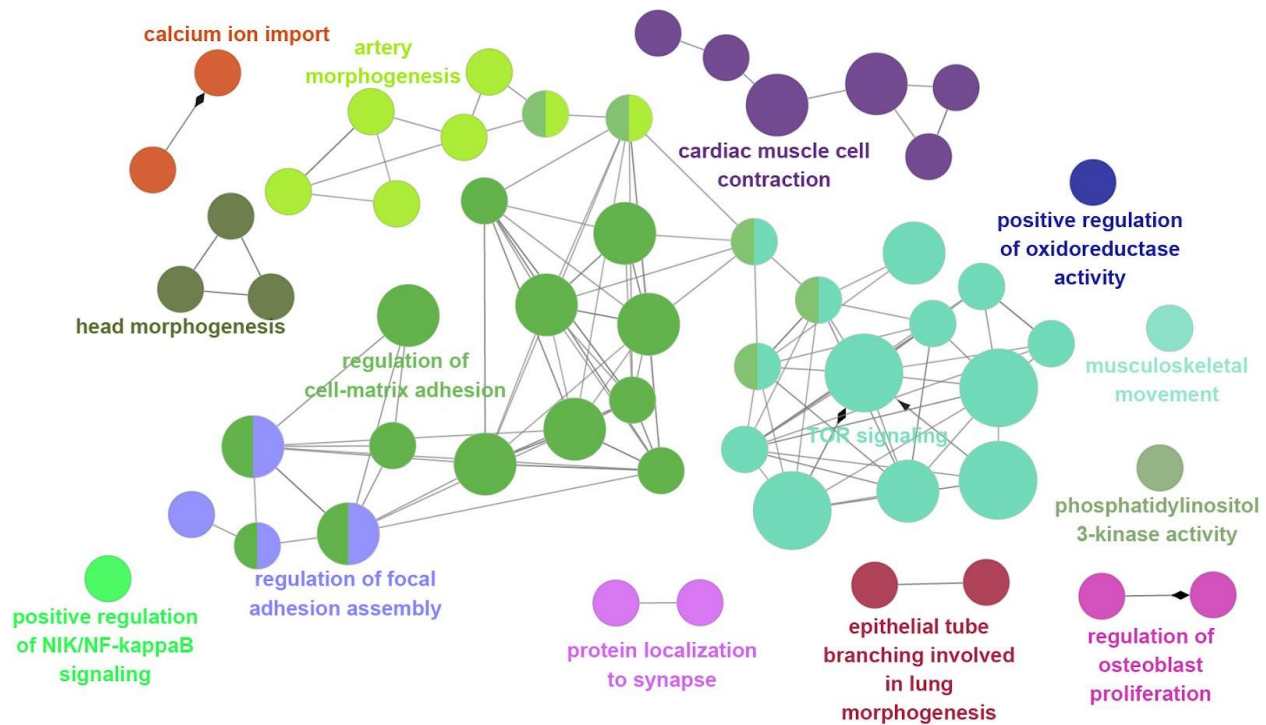
784
785
786
787
788
789
790

Extended Data Fig. 2 Mutational signature analysis through Mutalisk shows cell-division-related clock-like signatures in the MCD cohort. SBS5 (39.1%) and SBS1 (33%) are clock-like mutational signatures. SBS1 especially correlates with cell-division and mitosis of stem cells.



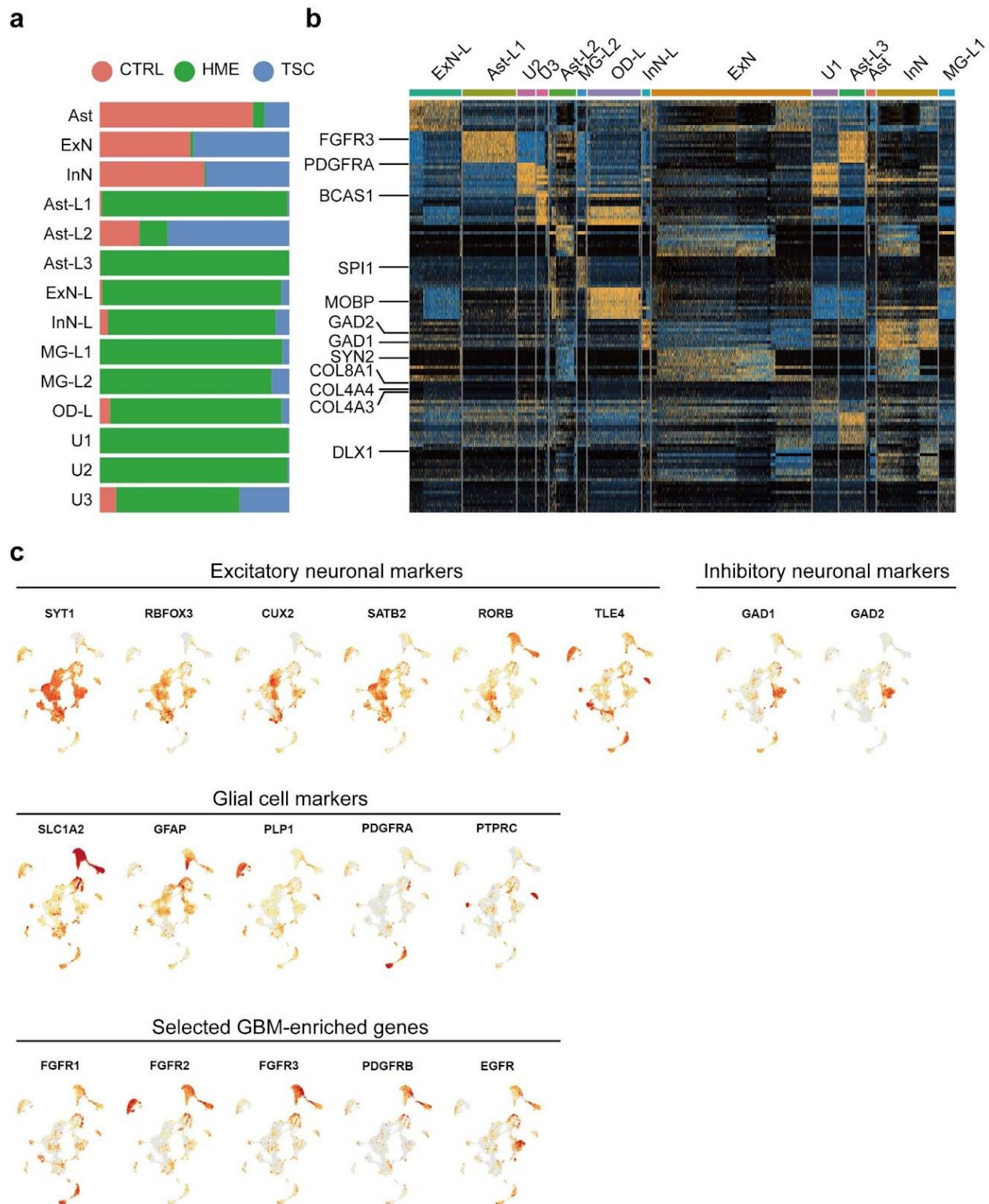
791
 792 **Extended Data Fig. 3 The locations of the selected MCD variants.** (a) The location of two
 793 recurrent variant calls are at the same position between coiled-coil domain (CC) and the first
 794 SAM domain (S) of Liprin- $\alpha 4$. (b) Two different variants in SERCA1. p.R524C mutation is at
 795 the nucleotide ATP-binding (N) domain, whereas the p.A846T variant is in the 7th
 796 transmembrane (M7) domain. A: Actuator domain, P: Phosphorylation domain, M:
 797 Transmembrane domain. (c) Left: The location of p.H226R variant in RAGA protein. GTPase:
 798 GTPase domain, CRD: C-terminal roadblock domain. Right: UCSC genome browser screenshot

799 describing that p.H226 is conserved site across all vertebrates. (d) The location of p.R38Q
800 variant in the N-terminal region before BTB (Broad-Complex, Tramtrack and Bric a brac)
801 domain of KLHL22. (e) A variant in the S1 domain of NR2C. S1 and S2 together make ligand-
802 binding domain (LBD), the target of glutamate. ATD: Amino terminal domain.
803



804
805
806
807
808
809
810
811

Extended Data Fig. 4 The ClueGO analysis using the MCD genes result identifies the biological processes and molecular pathways. The main cluster is related to TOR signaling, regulation of cell-matrix adhesion, regulation of focal adhesion assembly, artery morphogenesis. Notably, there are also isolated clusters which were not covered in previous studies, for example, cardiac muscle cell contraction, calcium ion import and protein localization to synapse. Term p-value with Bonferroni correction was reflected in node size (Large: $p < 0.0005$, medium: $p < 0.05$, small: $p < 0.1$).



812

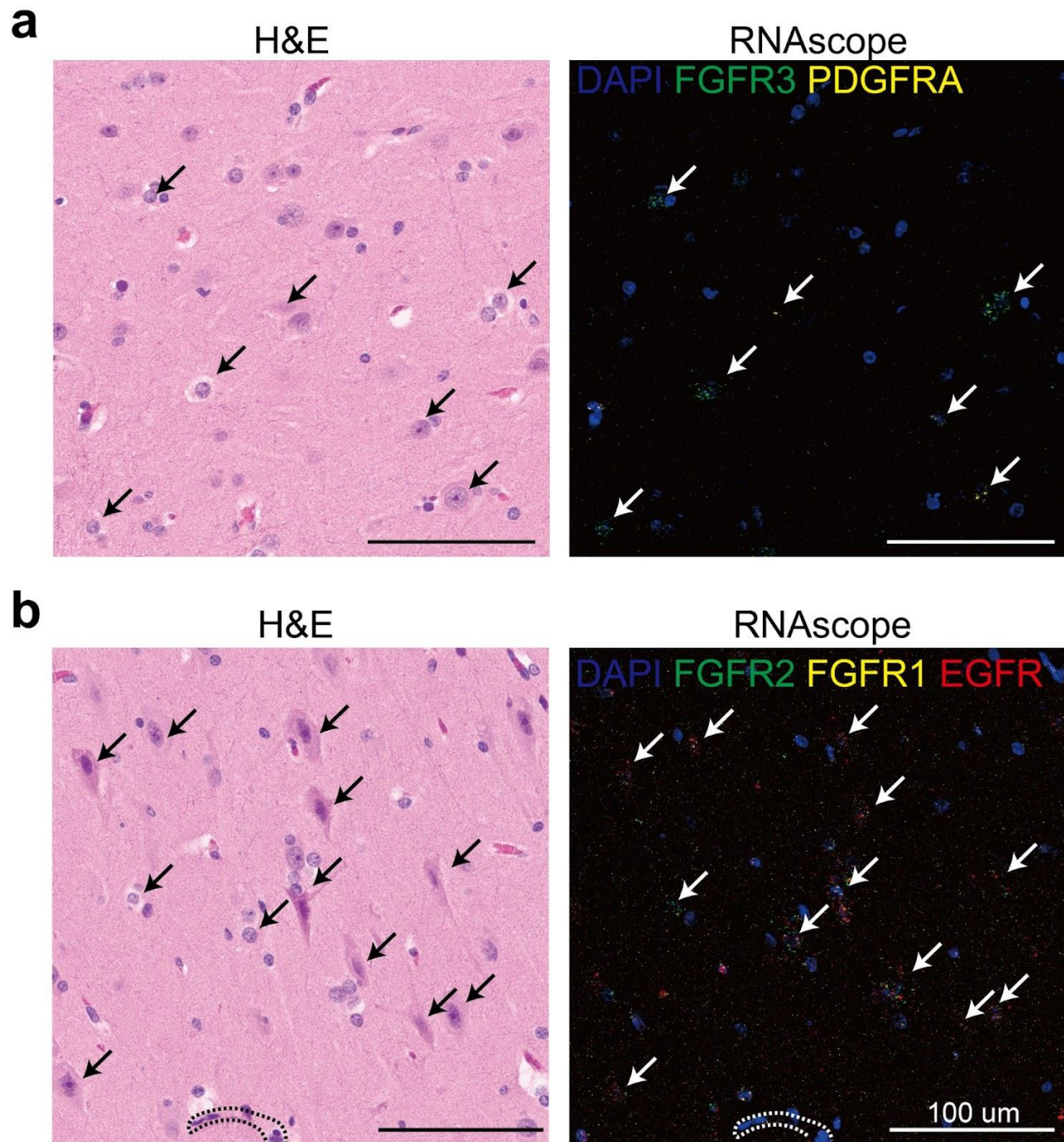
813 **Extended Data Fig. 5 Cell-type identification by DEGs and known marker gene expression**

814 **in the MCD snRNAseq dataset.** (a) MCD prefix was used for the clusters that have less than

815 25 % of control origin. (b) DEG analysis using FindAllMarker function in Seurat v4 package.

816 Top 10 genes for each cluster were presented. Several notable genes helping to define major cell

817 types were labeled at the left side. Note that *FGFR3* and *PDGFRA* are up-regulated in Ast-L1/3
818 and U1/2/3, respectively, implying that these genes can be the markers for MCD-dominant
819 clusters. (c) Selected markers for major cell types in the human cortex. *CUX1*, *CUX2* for upper
820 layer excitatory neuronal markers, *SATB2* for layer 4 excitatory neuronal marker, *RORB*,
821 *FEZF2*, *BCL11B*, *FOXP2*, *ROBO2* for deep layer specific markers, *GAD1*, *GAD2*, *DLX6*, *RELN*
822 for inhibitory neuronal markers, *GFAP*, *SLC1A2*, *SLC1A3*, *MMD2* for astrocyte markers, *PTPRC*
823 for microglial marker, *OLIG1*, *OLIG2*, *MOBP*, *PLP1* for oligodendrocyte markers, *FGFR1*,
824 *FGFR2*, *FGFR3*, *PDGFRB*, *EGFR* for the selected GBM-enriched genes covering subsets of
825 MCD-enriched clusters.
826



827

828

829 **Extended Data Fig. 6 The validation of snRNAseq result from HME-6593 shows MCD**

830 **dominant clusters are highly correlate with dysplastic cells in MCD.** (a) H&E staining (left)

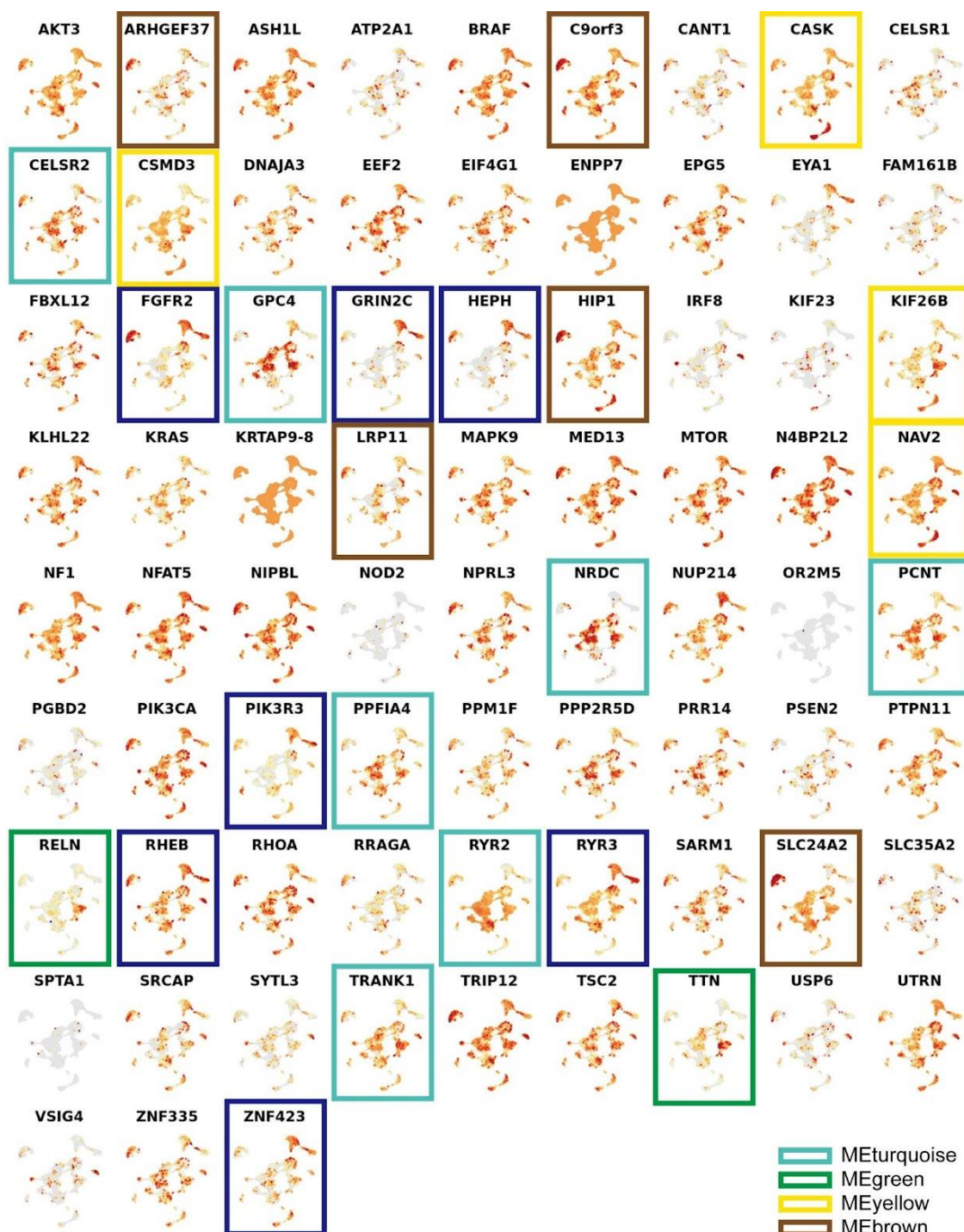
831 and RNAscope (right) staining results with several MCD-dominant markers (*FGFR2*, *FGFR1*,

832 *EGFR*) in the same formaldehyde-embedded-paraffin-fixed section. (b) H&E and RNAscope

833 result with another section with different RNA probes (*FGFR3* and *PDGFRA*) enriched in MCD

834 clusters. Dashed lines indicate blood vessels. White/black arrows are pointing to the dysplastic

cells.



835
 836 **Extended Data Fig. 7 Expression patterns of individual MCD genes in the MCD snRNAseq**
 837 **dataset.** The gene members of each eigen module shown in Fig. 6d were colored according to
 838 the name of a given eigengene.
 839

840 **Focal Cortical Dysplasia Neurogenetics Consortium (Additional Members)**

841

842 Dr. Yasemin Alanay, Division of Pediatric Genetics, Acibadem Hospital, Istanbul, Turkey

843 Dr. Seema Kapoor, Division of Genetics, Genetic & Metabolic Lab, Lok Nayak Hospital &

844 Maulana Azad Medical Center, Pakistan

845 Dr. Georgia Ramantani, Dr. Thomas Feuerstein, Albert-Ludwigs University, Freiburg, Germany

846 Dr. Ingmar Blumcke, Dr. Robyn Busch, Dr. Zhong Ying, Department of Neuropathology,

847 University Hospital Erlangen, Germany

848 Dr. Vadym Biloshytsky, Dr. Kostiantyn Kostiuk, Dr. Eugene Pedachenko, A. Romodanov

849 Institute of Neurosurgery, Kyiv, Ukraine

850 Dr. Marilyn Jones, Diane Masser-Frye, Rady Children's Hospital, San Diego, CA

851 Dr. St éphanie Baulac, Dr. Sara Baldassari, Sorbonne University, Paris Brain Institute (ICM),

852 Inserm, CNRS, AP-HP, Pitié-Salpêtrière Hospital, Paris, France

853 Dr. Ingo Helbig, Dr. Benjamin C. Kennedy, Division of Neurology, Children's Hospital

854 Philadelphia, PA

855 Dr. Judy Liu, Dr. Felix Chan, Department of Molecular Biology, Cell Biology, and Biochemistry,

856 Department of Neurology, Brown University, RI

857 Dr. Darcy Krueger, Department of Clinical Pediatrics and Neurology, Cincinnati Children's

858 Hospital, OH

859 Dr. Richard Frye, Dr. Angus Wilfong, Dr. David Adelson, Barrow Neurological Institute at

860 Phoenix Children's Hospital, U Arizona College of Medicine, Phoenix, AZ

861 Dr. William Gaillard, Dr. Chima Oluigbo, Children's National Hospital, Washington DC

862 Dr. Anne Anderson, Dept of Pediatrics, Baylor College of Medicine, Texas Children's Hospital,

863 Houston, TX

864

865 gmathern@ucla.edu, jwchang@mednet.ucla.edu, renzo.guerrini@meyer.it, yalanay@gmail.com,

866 drseemakapoor@gmail.com, Thomas.feuerstein@uniklinik-freiburg.de,

867 georgia.ramantani@kispi.uzh.ch, hipo0207@yuhs.ac, carola.haas@uniklinik-freiburg.de,

868 catharina.donkels@uniklinik-freiburg.de, takahashi-ped@umin.ac.jp, hrmachad@gmail.com,

869 camila.neurociencias@gmail.com, wilsonjr@usp.br, gurnettc@neuro.wustl.edu,

870 gardnerc@wustl.edu", ingmar.blumcke@uk-erlangen.de, vabil@i.ua, ssattar@health.ucsd.edu,

871 dgonda@rchsd.org, mnespeca@rchsd.org, mjone@rchsd.org, dmasser-frye@rchsd.org,

872 roberthchen3@gmail.com, jinwu.tsai@gmail.com, stephanie.baulac@sorbonne-universite.fr,

873 sara.baldassari@icm-institute.org, HELBIGI@chop.edu, KENNEDYBC@chop.edu,

874 judy_liu@brown.edu, felix_chan@brown.edu, darcy.kreuger@cchmc.org,

875 rfrye@phoenixchildrens.com, awilfong@phoenixchildrens.com,

876 dadelson@phoenixchildrens.com, WGAILLAR@childrensnational.org,

877 COluigbo@childrensnational.org, annea@bcm.edu,

878

879 **Brain Somatic Mosaicism Network**

880 Boston Children's Hospital: Alice Lee, August Yue Huang, Alissa D'Gama, Caroline Dias,
881 Christopher A. Walsh, Eduardo Maury, Javier Ganz, Michael Lodato, Michael Miller, Pengpeng
882 Li, Rachel Rodin, Rebeca Borges-Monroy, Robert Hill, Sara Bizzotto, Sattar Khoshkhou, Sonia
883 Kim, Zinan Zhou

884 Harvard University: Alice Lee, Alison Barton, Alon Galor, Chong Chu, Craig Bohrsen, Doga
885 Gulhan, Eduardo Maury, Elaine Lim, Euncheon Lim, Giorgio Melloni, Isidro Cortes, Jake Lee,
886 Joe Luquette, Lixing Yang, Maxwell Sherman, Michael Coulter, Minseok Kwon, Peter J. Park,
887 Rebeca Borges-Monroy, Semin Lee, Sonia Kim, Soo Lee, Vinary Viswanadham, Yanmei Dou

888 Icahn School of Medicine at Mt. Sinai: Andrew J. Chess, Attila Jones, Chaggai Rosenbluh,
889 Shahram Akbarian

890 Kennedy Krieger Institute: Ben Langmead, Jeremy Thorpe, Sean Cho

891 Lieber Institute for Brain Development: Andrew Jaffe, Apua Paquola, Daniel Weinberger,
892 Jennifer Erwin, Jooheon Shin, Michael McConnell, Richard Straub, Rujuta Narurkar

893 Mayo Clinic: Alexej Abyzov, Taejeong Bae, Yeongjun Jang, Yifan Wang

894 NIMH: Anjene Addington, Geetha Senthil

895 Sage Bionetworks: Cindy Molitor, Mette Peters

896 Salk Institute for Biological Studies: Fred H. Gage, Meiyang Wang, Patrick Reed, Sara Linker

897 Stanford University: Alexander Urban, Bo Zhou, Reenal Pattni, Xiaowei Zhu

898 Universitat Pompeu Fabra: Aitor Serres Amero, David Juan, Inna Povolotskaya, Irene Lobon,
899 Manuel Solis Moruno, Raquel Garcia Perez, Tomas Marques-Bonet

900 University of Barcelona: Eduardo Soriano

901 University of California, Los Angeles: Gary Mathern

902 University of California, San Diego: Danny Antaki, Dan Averbuj, Eric Courchesne, Joseph G.
903 Gleeson, Laurel L. Ball, Martin W. Breuss, Subhojit Roy, Xiaoxu Yang, Changuk Chung

904 University of Michigan: Chen Sun, Diane A. Flasch, Trenton J. Frisbie Trenton, Hui C.
905 Kopera, Jeffrey M. Kidd, John B. Moldovan, John V. Moran, Kenneth Y. Kwan, Ryan E. Mills,
906 Sarah B. Emery, Weichen Zhou, Xuefang Zhao

907 University of Virginia: Aakrosh Ratan

908 Yale University: Adriana Cherskov, Alexandre Jourdon, Flora M. Vaccarino, Liana Fasching,
909 Nenad Sestan, Sirisha Pochareddy, Soraya Scuder

910
911 Christopher.Walsh@childrens.harvard.edu, peter_park@hms.harvard.edu,
912 nenad.sestan@yale.edu, gage@salk.edu, drweinberger@libd.org, moranj@umich.edu,
913 flora.vaccarino@yale.edu, abyzov.alexej@mayo.edu, jogleeson@health.ucsd.edu,
914 gmathern@ucla.edu, ecourchesne1949@gmail.com, s1roy@ucsd.edu, andrew.chess@mssm.edu,
915 schahram.akbarian@mssm.edu, pevsner@kennedykrieger.org, mette.peters@sagebase.org,
916 cindy.molitor@sagebase.org,
917

918 References

- 919 1. Leventer, R.J., Guerrini, R. & Dobyns, W.B. Malformations of cortical development and epilepsy. *Dialogues*
920 *Clin Neurosci* **10**, 47-62 (2008).
- 921 2. Barkovich, A.J., Dobyns, W.B. & Guerrini, R. Malformations of cortical development and epilepsy. *Cold*
922 *Spring Harb Perspect Med* **5**, a022392 (2015).
- 923 3. Blumcke, I. *et al.* The clinicopathologic spectrum of focal cortical dysplasias: a consensus classification
924 proposed by an ad hoc Task Force of the ILAE Diagnostic Methods Commission. *Epilepsia* **52**, 158-74 (2011).
- 925 4. Choi, S.A. & Kim, K.J. The Surgical and Cognitive Outcomes of Focal Cortical Dysplasia. *J Korean*
926 *Neurosurg Soc* **62**, 321-327 (2019).
- 927 5. Poduri, A. *et al.* Somatic activation of AKT3 causes hemispheric developmental brain malformations. *Neuron*
928 **74**, 41-8 (2012).
- 929 6. Lee, J.H. *et al.* De novo somatic mutations in components of the PI3K-AKT3-mTOR pathway cause
930 hemimegalencephaly. *Nat Genet* **44**, 941-5 (2012).
- 931 7. Baldassari, S. *et al.* Dissecting the genetic basis of focal cortical dysplasia: a large cohort study. *Acta*
932 *Neuropathol* **138**, 885-900 (2019).
- 933 8. Sim, N.S. *et al.* Precise detection of low-level somatic mutation in resected epilepsy brain tissue. *Acta*
934 *Neuropathol* **138**, 901-912 (2019).
- 935 9. Dou, Y. *et al.* Accurate detection of mosaic variants in sequencing data without matched controls. *Nat*
936 *Biotechnol* **38**, 314-319 (2020).
- 937 10. Yang, X. *et al.* DeepMosaic: Control-independent mosaic single nucleotide variant detection using deep
938 convolutional neural networks. *bioRxiv* (2021).
- 939 11. Huang, A.Y. *et al.* MosaicHunter: accurate detection of postzygotic single-nucleotide mosaicism through
940 next-generation sequencing of unpaired, trio, and paired samples. *Nucleic Acids Res* **45**, e76 (2017).
- 941 12. Wang, Y. *et al.* Comprehensive identification of somatic nucleotide variants in human brain tissue. *Genome*
942 *Biol* **22**, 92 (2021).
- 943 13. Breuss, M.W. *et al.* Autism risk in offspring can be assessed through quantification of male sperm mosaicism.
944 *Nat Med* **26**, 143-150 (2020).
- 945 14. Yang, X. *et al.* Developmental and temporal characteristics of clonal sperm mosaicism. *Cell* **184**, 4772-4783
946 e15 (2021).
- 947 15. Garcia, C.A.B. *et al.* mTOR pathway somatic variants and the molecular pathogenesis of
948 hemimegalencephaly. *Epilepsia Open* **5**, 97-106 (2020).
- 949 16. Pelorosso, C. *et al.* Somatic double-hit in MTOR and RPS6 in hemimegalencephaly with intractable epilepsy.
950 *Hum Mol Genet* **28**, 3755-3765 (2019).
- 951 17. Breuss, M.W. *et al.* Somatic mosaicism in the mature brain reveals clonal cellular distributions during cortical
952 development. *Nature* (2022).
- 953 18. Bae, T. *et al.* Somatic mutations reveal hypermutable brains and are associated with neuropsychiatric
954 disorders. *medRxiv* (2022).
- 955 19. Bozic, I. *et al.* Accumulation of driver and passenger mutations during tumor progression. *Proc Natl Acad*
956 *Sci U S A* **107**, 18545-50 (2010).
- 957 20. Alexandrov, L.B. *et al.* The repertoire of mutational signatures in human cancer. *Nature* **578**, 94-101 (2020).
- 958 21. Kim, M. & Costello, J. DNA methylation: an epigenetic mark of cellular memory. *Exp Mol Med* **49**, e322
959 (2017).
- 960 22. Szklarczyk, D. *et al.* STRING v11: protein-protein association networks with increased coverage, supporting

- 961 functional discovery in genome-wide experimental datasets. *Nucleic Acids Res* **47**, D607-D613 (2019).
- 962 23. Bedrosian, T.A. *et al.* Detection of brain somatic variation in epilepsy-associated developmental lesions.
- 963 *medRxiv* (2021).
- 964 24. Lai, D. *et al.* Somatic mutation involving diverse genes leads to a spectrum of focal cortical malformations.
- 965 *medRxiv* (2021).
- 966 25. Tarabeux, J. *et al.* Rare mutations in N-methyl-D-aspartate glutamate receptors in autism spectrum disorders
- 967 and schizophrenia. *Transl Psychiatry* **1**, e55 (2011).
- 968 26. Bezprozvanny, I. Calcium signaling and neurodegenerative diseases. *Trends Mol Med* **15**, 89-100 (2009).
- 969 27. Su, M.Y. *et al.* Hybrid Structure of the RagA/C-Ragulator mTORC1 Activation Complex. *Mol Cell* **68**, 835-
- 970 846 e3 (2017).
- 971 28. Chen, J. *et al.* KLHL22 activates amino-acid-dependent mTORC1 signalling to promote tumorigenesis and
- 972 ageing. *Nature* **557**, 585-589 (2018).
- 973 29. Behar, T.N. *et al.* Glutamate acting at NMDA receptors stimulates embryonic cortical neuronal migration. *J*
- 974 *Neurosci* **19**, 4449-61 (1999).
- 975 30. Paoletti, P., Bellone, C. & Zhou, Q. NMDA receptor subunit diversity: impact on receptor properties, synaptic
- 976 plasticity and disease. *Nat Rev Neurosci* **14**, 383-400 (2013).
- 977 31. Strehlow, V. *et al.* GRIN2A-related disorders: genotype and functional consequence predict phenotype. *Brain*
- 978 **142**, 80-92 (2019).
- 979 32. Prickett, T.D. & Samuels, Y. Molecular pathways: dysregulated glutamatergic signaling pathways in cancer.
- 980 *Clin Cancer Res* **18**, 4240-6 (2012).
- 981 33. Ruvinsky, I. & Meyuhos, O. Ribosomal protein S6 phosphorylation: from protein synthesis to cell size.
- 982 *Trends Biochem Sci* **31**, 342-8 (2006).
- 983 34. Sumimoto, H., Imabayashi, F., Iwata, T. & Kawakami, Y. The BRAF-MAPK signaling pathway is essential
- 984 for cancer-immune evasion in human melanoma cells. *J Exp Med* **203**, 1651-6 (2006).
- 985 35. Ornitz, D.M. & Itoh, N. The Fibroblast Growth Factor signaling pathway. *Wiley Interdiscip Rev Dev Biol* **4**,
- 986 215-66 (2015).
- 987 36. Chen, X. *et al.* TNF-alpha-Induced NOD2 and RIP2 Contribute to the Up-Regulation of Cytokines Induced
- 988 by MDP in Monocytic THP-1 Cells. *J Cell Biochem* **119**, 5072-5081 (2018).
- 989 37. Yates, T.M. *et al.* SLC35A2-related congenital disorder of glycosylation: Defining the phenotype. *Eur J*
- 990 *Paediatr Neurol* **22**, 1095-1102 (2018).
- 991 38. Paganini, C. *et al.* Calcium activated nucleotidase 1 (CANT1) is critical for glycosaminoglycan biosynthesis
- 992 in cartilage and endochondral ossification. *Matrix Biol* **81**, 70-90 (2019).
- 993 39. Lee, N. *et al.* Neuronal migration disorders: positron emission tomography correlations. *Ann Neurol* **35**, 290-
- 994 7 (1994).
- 995 40. Kim, Y.H. *et al.* Neuroimaging in identifying focal cortical dysplasia and prognostic factors in pediatric and
- 996 adolescent epilepsy surgery. *Epilepsia* **52**, 722-7 (2011).
- 997 41. Nowakowski, T.J. *et al.* Spatiotemporal gene expression trajectories reveal developmental hierarchies of the
- 998 human cortex. *Science* **358**, 1318-1323 (2017).
- 999 42. Coe, B.P. *et al.* Neurodevelopmental disease genes implicated by de novo mutation and copy number
- 1000 variation morbidity. *Nat Genet* **51**, 106-116 (2019).
- 1001 43. Ridley, A.J. *et al.* Cell migration: integrating signals from front to back. *Science* **302**, 1704-9 (2003).
- 1002 44. Brini, M., Cali, T., Ottolini, D. & Carafoli, E. Neuronal calcium signaling: function and dysfunction. *Cell*
- 1003 *Mol Life Sci* **71**, 2787-814 (2014).
- 1004 45. Lamparello, P. *et al.* Developmental lineage of cell types in cortical dysplasia with balloon cells. *Brain* **130**,
- 1005 2267-76 (2007).
- 1006 46. Englund, C., Folkerth, R.D., Born, D., Lacy, J.M. & Hevner, R.F. Aberrant neuronal-glia differentiation in
- 1007 Taylor-type focal cortical dysplasia (type IIA/B). *Acta Neuropathol* **109**, 519-33 (2005).
- 1008 47. Kim, S. *et al.* Strelka2: fast and accurate calling of germline and somatic variants. *Nat Methods* **15**, 591-594
- 1009 (2018).
- 1010 48. Benjamin, D. *et al.* Calling Somatic SNVs and Indels with Mutect2. *bioRxiv* (2019).
- 1011 49. Yang, X. *et al.* Genomic mosaicism in paternal sperm and multiple parental tissues in a Dravet syndrome
- 1012 cohort. *Sci Rep* **7**, 15677 (2017).
- 1013 50. Untergasser, A. *et al.* Primer3Plus, an enhanced web interface to Primer3. *Nucleic Acids Res* **35**, W71-4
- 1014 (2007).

- 1015 51. Untergasser, A. *et al.* Primer3--new capabilities and interfaces. *Nucleic Acids Res* **40**, e115 (2012).
1016 52. Lee, J. *et al.* Mutalisk: a web-based somatic MUTation AnaLyIS toolKit for genomic, transcriptional and
1017 epigenomic signatures. *Nucleic Acids Res* **46**, W102-W108 (2018).
1018 53. Bindea, G. *et al.* ClueGO: a Cytoscape plug-in to decipher functionally grouped gene ontology and pathway
1019 annotation networks. *Bioinformatics* **25**, 1091-3 (2009).
1020 54. Koizumi, H., Tanaka, T. & Gleeson, J.G. Doublecortin-like kinase functions with doublecortin to mediate
1021 fiber tract decussation and neuronal migration. *Neuron* **49**, 55-66 (2006).
1022 55. Wang, F. *et al.* RNAscope: a novel in situ RNA analysis platform for formalin-fixed, paraffin-embedded
1023 tissues. *J Mol Diagn* **14**, 22-9 (2012).
1024